THREE-DIMENSIONAL FLOW FIELD

IN ROCKET PUMP INDUCERS

(NASA-CR-140916) THREE DIMENSIONAL FLOW FIELD IN ROCKET PUMP INDUCERS. PART 2: MEAN FLOW AND TURBULENCE CHARACTERISTICS INSIDE THE ROTOR PASSAGE, AND THEORETICAL ANALYSIS (Pennsylvania State Univ.) 47 p HC G3/34

N75-14992

Unclas
07054

Part 2*: Mean Flow and Turbulence Characteristics Inside the Rotor Passage, and Theoretical Analysis

B. Lakshminarayana** and C. A. Gorton***
Department of Aerospace Engineering
The Pennsylvania State University
University Park, PA 16802

*Part 1 of this paper was published in J. Fluids Engineering, p. 567-578, December 1973. This work was also supported by National Aeronautics and Space Administration through the Grant NGL 39-009-007 with technical management by W. R. Britsch of NASA Lewis Research Center.

**Professor, Mem ASME

***Presently Aerospace Engineer, Naval Air Systems Command, Washington, D.C.

ABSTRACT

This paper reports the measurement and prediction of three dimensional flow field in an axial flow inducer operating at a flow coefficient of 0.065 with air as the test medium. The experimental investigations included measurements of the blade static pressure and blade limiting streamline angle, and measurement of the three components of mean velocity, turbulence intensities and turbulence stresses at locations inside the inducer blade passage utilizing a rotating three-sensor hotwire probe. Analytical investigations were conducted to predict the three-dimensional inviscid flow and to approximately predict the three-dimensional viscid flow by incorporating the dominant viscous terms into the exact equations. Radial velocities are found to be of the same order as axial velocities and total relative velocity distributions indicate a substantial velocity deficiency near the tip at mid-passage. High turbulence intensities and turbulence stresses are concentrated within this core region. Evidence of boundary layer interactions, blade blockage effects, radially inward flows, annulus wall effects and backflows are all found to exist within the long, narrow passages of the inducer, emphasizing the complex nature of inducer flow which makes accurate prediction of the flow behavior extremely difficult.

NOMENCLATURE

C	Local blade chord
C_f	Skin friction coefficient
F	Viscous forces
h	Static head
LE,TE	Leading and trailing edges respectively
p	Static pressure
Pr	Pressure surface
Q_R	Total relative velocity (in experimental results non-dimensionalized with respect to U_b).
R	Non-dimensionalized radius (= r/r_t)
r,θ,Z	Rotating cylindrical coordinate system (Fig. 1)
R_e	Reynolds number ($\bar{Q}_R$ r/ν)
r	Local radius
s,n,r	Coordinates (See Fig. 1)
Su	Suction surface
S	Circumferential distance from suction surface non-dimensionalized by local blade spacing (distance between pressure and suction surfaces).
U,V,W	Mean relative velocity components in the r, θ, Z directions respectively (in experimental results non-dimensionalized with respect to U_b) Fig. 1
U_b	Blade tip speed (= $r_t\Omega$)
u,v,w	Fluctuating relative velocity components in the r, θ, Z directions respectively (in experimental results, non-dimensionalized with respect to Q_R)
X	Distance along the chord measured from leading edge
V_θ	Absolute tangential velocity
α	Blade limiting streamline angle (Fig. 1)
β	Flow angle (Fig. 1)

NOMENCLATURE (continued)

ρ	Fluid density
τ	Shear stress
ψ_s	Static head coefficient (= $2g\ h/U_b^2$)
Ω	Angular velocity of inducer

Superscripts

-	Time-averaged or passage-averaged quantity

Subscripts

t	Refers to values at the inducer tip
r,θ,z	Components in r, θ, z directions (Fig. 1)
s,n,r	Components in s, n, r directions (Fig. 1)

INTRODUCTION

The investigations reported in an earlier paper (1) is continued to obtain an accurate knowledge of the three dimensional mean flow and turbulence characteristics inside the passage of an axial flow inducer. The measurements, carried out with a rotating hot wire probe, and analysis, based on the exact solution of the equations of motion, has given a great insight into the flow characteristics, hitherto unknown, in this as well as other types of turbomachinery.

THEORETICAL ANALYSIS

Exact Inviscid Analysis:

Cooper and Bosch (2) have developed a method of obtaining the exact inviscid solution of the inducer flow field. Their three-dimensional analysis employs an iterative numerical procedure to solve the equations of motion expressed in finite-difference form. Cooper and Bosch program was subsequently modified by Poncet and Lakshminarayana (3) to include the trailing edge condition and by Gorton (4) to improve the convergence time. It has also been extended to include a viscid solution capability based on empirically determined blade skin friction coefficients.

The nonlinear partial differential equations governing the flow in a rotating cylindrical coordinate system r, θ, z (Fig. 1) are:

r momentum: $$\frac{1}{\rho}\frac{\partial p}{\partial r} + U\frac{\partial U}{\partial r} + \frac{V}{r}\frac{\partial U}{\partial \theta} + W\frac{\partial U}{\partial z} - \frac{1}{r}(V + r\Omega)^2 + F_r = 0 \qquad (1)$$

θ momentum: $$\frac{1}{\rho r}\frac{\partial p}{\partial \theta} + U\frac{\partial V}{\partial r} + \frac{V}{r}\frac{\partial V}{\partial \theta} + W\frac{\partial V}{\partial z} + \frac{UV}{r} + 2U\Omega + F_\theta = 0 \qquad (2)$$

z momentum: $$\frac{1}{\rho}\frac{\partial p}{\partial z} + U\frac{\partial W}{\partial r} + \frac{V}{r}\frac{\partial W}{\partial \theta} + W\frac{\partial W}{\partial z} + F_z = 0 \qquad (3)$$

continuity: $$\frac{U}{r} + \frac{\partial U}{\partial r} + \frac{1}{r}\frac{\partial V}{\partial \theta} + \frac{\partial W}{\partial z} = 0 \qquad (4)$$

In the Cooper-Bosch method, the above equations are rearranged to give residuals which are reduced to zero by a relaxation procedure. The total residual (RT) of one relaxation cycle is calculated by

$$RT = \sum_{i=1}^{IMAX}\sum_{j=1}^{JMAX}\sum_{k=1}^{KMAX}\left[(R1)^2 + (R2)^2 + (R3)^2 + (R4)^2\right]_{i,j,k} \qquad (5)$$

where R1, R2, R3 and R4 are the residuals calculated for the three momentum equations (Equations 1 to 3) and the continuity equation, and IMAX, JMAX and KMAX are the number of grid stations in the radial, tangential and axial directions which are used in the numerical analysis. From this, the total RMS (root mean square) residual is defined as

$$RMS = \sqrt{\frac{(RT)}{4\cdot(IMAX)\cdot(JMAX)\cdot(KMAX)}} \qquad (6)$$

and is thus a measure of the degree of convergence between the iterated solution and the exact solution. The boundary condition to be satisfied on the hub, annulus walls and the blade surfaces is $\vec{Q}_R \cdot \vec{n} = 0$, where $\vec{n}$ is the direction normal to the channel boundaries and $\vec{Q}_R$ is the total relative velocity.

In applying Cooper-Bosch program to the Penn State inducer, the flow is assumed to be incompressible, and a grid of 7 x 7 x 26 is chosen to represent the blade passage. The flow geometry is shown in Fig. 1.

The first of the 26 axial stations corresponds to the upstream through-flow boundary where the initial conditions are applied. The last four axial stations correspond to the downstream flow-through boundary, and extend to about one-fifth of the chord length downstream of the trailing edge. With $\vec{Q}_R \cdot \vec{n} = 0$ to be satisfied on these stagnation stream surfaces, the set of boundary conditions for the problem is complete.

For increased efficiency, the program written by Cooper and Bosch (2) has been compiled under a Fortran IV H level optimization procedure which reduces the time required for repetitive calculations. The next approach for the speedier solution of the governing flow equations is the optimization of the input parameters of velocity and pressure which would allow faster convergence to the three-dimensional solution. Cooper and Bosch (2) have derived an approximate solution to be used as an initial input to the exact program. This method derives the blade-to-blade average quantities using axisymmetric equations, then uses these quantities in a blade-to-blade solution of an integrated form of the scalar momentum equation in the tangential direction. The flow parameters derived by this method were used in Ref. 3. However, an alternate method of developing the initial input parameters is to estimate the velocities and static pressures inside the passage using the two dimensional solution. The method adopted here is to use the Douglas-Neumann program described in Ref. 5. The two dimensional analysis is modified to include the effect of converging walls using the analysis of Ref. 6.

Using the input parameters of velocity and pressure derived from the preceeding analysis results in a lower total RMS (root mean square) residual than with the previous method of initializing the input variables. As an example, the final RMS residual for the inviscid results of Ref. 3 was

0.12450 after 68 relaxation cycles, whereas a similar value is obtained using the present analysis in 10 relaxation cycles. This amounts to a considerable saving in computer time. Twenty-five iteration cycles has reduced the RMS residual to 0.10579, indicating that a faster convergence to the solution should be possible.

In a further attempt to decrease the convergence time, the exit flow angle was allowed to change depending upon the tangential and axial velocities calculated at the inducer trailing edge. Since the exact downstream boundaries are not known in this type of problem, it was hoped that by allowing the downstream boundaries to adjust themselves and thereby unload the blade trailing edge, a more exact definition of the downstream streamlines would result in lower RMS residuals. Cooper and Bosch suggest a similar technique as a means of reducing RMS residuals in their recommendations for future work.

Since the extension of the stagnation stream surfaces downstream have been constructed to be uniformly periodic with a spacing of $2\pi/N$ (N being the number of blades), the values of velocity and pressure at the downstream tangential channel boundaries should be equal. This condition is applied at the blade trailing edge after each iteration cycle. If the pressure and suction surface parameters differ with each other at the trailing edge grid point, the average value is used in the residual calculations. If the axial and/or tangential velocities at the trailing edge diverge significantly from the design values during the iteration process, then the flow exit angle, defined by $\beta = \tan^{-1} \frac{V}{W}$ at the trailing edge, is recalculated and is used to redefine the downstream stagnation stream surfaces. This method also has the advantage of automatically forcing the Kutta-Joukowski condition for the blade pressure distribution to be

satisfied. Changes made to the original Cooper-Bosch program including a listing of the computer program is given in Ref. 4.

Cooper and Bosch program was run for the three bladed configuration (Fig. 1) without the modification as well as with the modification forcing the pressure to be equal on both the pressure and suction surface at the trailing edge. The iterations were carried out for 24 cycles. The blade static pressures at the hub and tip radial locations are shown in Fig. 2. The modification close the pressure diagram perfectly. The predictions agree well with the experimental data. The hub wall static pressures were measured midway between the two blade surfaces and the annulus wall static pressures were derived from the static pressure taps located at various axial locations along the annulus wall. Hence the latter measurements are time averaged values.

Approximate Viscid Analysis:

In addition to the attempts to improve the convergence of the exact inviscid solution, a method of incorporating viscid effects into the governing equations of motion has also been investigated.

In the momentum equations used by Cooper and Bosch (Equation 1 to3), the following expressions for F_r, F_θ and F_z (the exact program variables for viscous loss terms) can be given as:

$$F_r = -\frac{1}{\rho}\left[\frac{\partial \tau_{r\theta}}{r\partial\theta} + \frac{\partial \tau_{rz}}{\partial z} + \frac{\partial \sigma_{rr}}{\partial r} + \frac{(\sigma_{rr} - \sigma_{\theta\theta})}{r}\right] \tag{7}$$

$$F_\theta = -\frac{1}{\rho}\left[\frac{\partial \sigma_{\theta\theta}}{r\partial\theta} + \frac{\partial \tau_{\theta z}}{\partial z} + \frac{\partial \tau_{\theta r}}{\partial r} + \frac{2}{r}\tau_{\theta r}\right] \tag{8}$$

$$F_z = -\frac{1}{\rho}\left[\frac{\partial \tau_{z\theta}}{r\partial\theta} + \frac{\partial \sigma_{zz}}{\partial z} + \frac{\partial \tau_{rz}}{\partial r} + \frac{\tau_{rz}}{r}\right] \tag{9}$$

Where,

$$\sigma_{\theta\theta} = -\overline{v^2},\ \tau_{\theta z} = -\overline{vw} = \tau_{z\theta}$$

$$\sigma_{rr} = -\overline{u^2},\ \tau_{rz} = -\overline{uw} = \tau_{zr}$$

$$\sigma_{zz} = -\overline{w^2},\ \tau_{\theta r} = -\overline{vu} = \tau_{r\theta}$$

Molecular viscosity terms have been neglected in these equations.

Since the stagger angle is very large, these viscous terms can be approximated by retaining the diminant terms as well as neglecting the normal shear stresses, resulting in:

$$F_r = -\frac{1}{\rho}\frac{\partial \tau_{rz}}{\partial z},\quad F_\theta = -\frac{1}{\rho}\frac{\partial \tau_{\theta z}}{\partial z},\quad F_z = -\frac{1}{\rho}\frac{\partial \tau_{z\theta}}{r\partial\theta} \tag{10}$$

The distribution of shear stress is assumed to be linear across the flow passage from pressure surface to suction surface (with zero at the midpassage). The values of wall shear stresses are assumed to be known from previous experimentation. Skin friction coefficient C_f for a four-blade flat plate helical channel is given in Ref. 7. The results, summarized in Fig. 3 are considered to be valid for the three-blade inducer under consideration. Interpolation of the curves in Fig. 3 for a given blade surface grid location under consideration gives a value of wall shear stress $\tau_w = C_f \cdot \frac{1}{2}\rho\,\bar{Q}_R^2$ for the appropriate Reynolds number $R_e = \bar{Q}_R \cdot r/\nu$ of the flow at that point, where $\bar{Q}_R$ is the average relative velocity across the flow passage as derived by the Cooper-Bosch relaxation procedure. The resultant turbulence stress at each grid point are thus calculated. The components along each coordinate direction is assumed to vary according to the ratio

of the corresponding local velocity component to total relative velocity. The derivatives are calculated by finite difference method according to equation 10.

An additional requirement placed on the viscid analysis is to satisfy the viscid boundary condition which requires that all components of velocity are zero at the blade surface. The changes to the original Cooper and Bosch exact program necessitated by the inclusion of the viscous loss terms are made in subroutines "MAIN", "DLOSS" and "RESID" of the Cooper-Bosch program and are given in Ref. 4. It should be emphasized here that this is a first attempt to solve the entire viscous equation for rotor passage and is a preliminary one in as much as the shear stress distributions are assumed. For more accurate analysis, one has to resort to turbulent energy equation with suitable turbulence modelling.

The input variables and formats for the modified viscid analysis program are identical to the original Cooper-Bosch program, with the exception of including a set of curves to define blade skin friction coefficient (C_f) vs. Reynolds number (R_e) for various reference tangential locations throughout the inducer channel. Preliminary running of the modified viscid program indicates an increase in computer time of approximately two to three times more than a corresponding inviscid analysis run. This increase in computation time is due to the calculation of the viscous loss terms F_r, F_θ and F_z at each grid point location throughout the duration of one relaxation cycle, which may involve several thousand iterations of the flow parameters in order to reduce the RMS residual from the previous cycle.

The Cooper-Bosch exact analysis program incorporating the modifications mentioned in this section was run for the three-bladed Penn State inducer geometry. Both inviscid and viscid cases were considered. The inviscid

program was run for approximately 75 relaxation cycles, resulting in a total RMS residual of 0.077. The viscid program was run for approximately 50 cycles and produced a total RMS residual of 0.200. Most of the contribution to the total RMS residual comes from the upstream and the leading edge stations. In the viscid program the residuals at the blade surfaces were large in addition to the above stations. At most other locations, the total residual (local) was verying from 10^{-2} to 10^{-4}. The results of the inviscid and viscid analyses will be discussed and compared with the experimental results later.

EXPERIMENTAL FACILITY AND PROGRAM

The experimental investigation was performed in a 0.915 m diameter axial flow inducer with three equally spaced blades. Design of the rotor and description of the facility is given in Ref. 8. The use of the three bladed inducer for the continued experimental investigation is a result of the conclusions reached in Ref. 1; namely it has appreciably better performance than a four bladed inducer tested at the same operating conditions. The inducer was operated at a flow coefficient of 0.065 at 450 RPM with air as the test medium. The Reynolds number based on tip radius was 7×10^5.

An extensive experimental investigation of the rotor blade static pressure distribution has been undertaken to help provide a check on the theoretical analysis and useful information for future theoretical development. A scanivalve, three channel pressure transfer device, slip ring unit were used to transmit pressures from rotor blade to a stationary manometer. The schematic of this set up is shown in Fig. 4. The blade static pressures were measured along quasi two dimensional stream surfaces at five radii shown in Fig. 5. The blade static pressures were measured at ten chordwise locations each on the blade pressure and suction surfaces. The coordinates of the measuring stations are tabulated in Ref. 4.

The measurement of the blade limiting streamline angle (α) (Fig. 1), which is the limiting position of the streamline as the blade surface is

approached, is a further attempt to define the flow phenomena within the blade boundary layer, including nature and magnitude of the radial flows and the direction of the wall shear stress. The information gained will help establish the extent of three-dimensionality in the inducer flow and will be valuable in developing a viscid theory for the prediction of rotating boundary layer characteristics. The blade measurement stations are identical to those used for the blade static pressure measurements. The method and equipment for measurement are essentially the same as that used in Ref. 9.

A triple sensor hot wire probe (rotating with the inducer) is used inside the passage to measure the three components of mean velocity, turbulent intensities and stresses. The governing equations, method, technique, instrumentation used and an estimate of the error involved are described fully in Ref. 10. The resultant voltage measurements from the hot wire were converted to mean velocities U, V, W and turbulence quantities $\overline{u^2}$, $\overline{v^2}$, $\overline{w^2}$, $\overline{uv}$, $\overline{uw}$ and $\overline{vw}$ from the hot wire calibration curves and the applicable hot wire equations (Ref. 10). Measurements were taken at two axial stations, corresponding to approximately 33% and 90% of the blade chord (Fig. 5). Various velocity measurements have been performed at these stations (Ref. 1) and thus a comparison of hot wire experimental results with these prior investigations are possible (Ref. 4). Six radial stations (R = 0.973, 0.945, 0.890, 0.781, 0.671, 0.548) at axial station A* and five radial stations (R = 0.973, 0.945, 0.890, 0.781, 0.671) at axial station B* were traversed at several tangential intervals within the blade passage in an attempt to get an accurate and detailed appraisal of the flow

---

*Axial stations referred to as A, B and C in this paper are same as stations 1, 2 and 3 in Fig. 1 of Ref. 1.

velocities, turbulence intensities and stresses in these regions. It was not possible, however, to obtain measurements close to the blade surface due to limitations caused by the blade curvature.

EXPERIMENTAL RESULTS AND COMPARISON WITH THEORY

Blade Static Pressure:

Experimental and theoretical results are plotted in Fig. 6 for the five radial passage locations defined previously. It should be reiterated that the measurement stations do not correspond to constant radii, since the annulus area is continuously varying. The measurement stations are shown in Fig. 5 and follows approximately the streamlines calculated from one dimensional consideration.

The inducer design characteristic of trailing edge loaded blade is apparent from the measured ψ_s distribution. The blade static pressures are negative only near the leading edge of the suction surface and this follows the design trend based on cavitation criteria. The measured values of ψ_s are found to be considerably different from the design values. The decrepancy is found to be maximum at the tip radius as shown in Fig. 6e. The design values are the ones assumed for deriving the blade profile from Wislicenus's (Ref. 8)'mean streamline method.' Even though the design incorporates the effect of change in axial velocity and the blade blockage, the use of correlations based on cascade results are inadequate. This serves as a caution for those who are contemplating using the 'mean streamline method' in designing unconventional blading. The experimental results indicate that the three dimensional inviscid effects are large. The flow near the tip, especially on the suction surface, is dominated by boundary layer effects (Figs. 6d and 6e).

As can be seen in Fig. 6, the inviscid predictions agree well with experiment especially from hub to mid-radius, where the viscid effects are small due to large migration of the blade boundary layer towards the tip (Ref. 9). The inviscid and viscid predictions are close at most of the radii. The greatest variation between the two predictions occur near the tip (Fig. 6e), where the viscous effects are dominant. The suction surface pressure distributions in this region predicted from the viscid analysis shows better agreement with the experiment than the inviscid analysis.

In Fig. 7a are shown the passage averaged static pressure measured (using a stationary probe at the exit) very near the trailing edge (Ref. 3) compared with the predictions. Near the hub, the inviscid theory is in better agreement and at other locations (except at the very tip), the viscid theory shows better agreement with the experiment. The radial variation of ψ_s are compared with theory in Fig. 7b for axial stations A and B shown in Fig. 5. The agreement between the theory and the experiment is very good, except at the very tip at station B.

It is clear that the viscous effect has no appreciable influence on the blade static pressure distribution from hub to mid-radius. But its effect on velocities and shear stresses are considerable as indicated later.

The measured and design static pressures are considerably different as shown in Fig. 7b for station A. The descrepancy at station B is found to be much worse (Ref. 4).

Limiting Streamline Angles:

The variation of the limiting streamline angle (α) with blade chord for each of the five radial measurement stations is shown in Fig. 8. The pressure surface distribution of α at the tip (radial station 5) indicates negative values of α (and, thus, radially inward flow) from leading edge

to mid-chord position. This tends to indicate the presence of the annulus wall boundary layer scraping effect which induces flow away from the tip. At all other radial stations, α increases continuously from leading edge to trailing edge. Near the hub trailing edge, α increases quite rapidly. The blade limiting streamline angles at both radial stations 1 and 2 appear to extrapolate beyond 90° at the trailing edge, which is an indication of the existence of backflow in this region. This is presumably brought about by large radially outward flow that exists in the wake immediately downstream of the trailing edge. This has a tendency to decrease axial velocity near the hub and thus induce backflows. At most axial locations, α decreases continuously from hub to tip. In several instances, this decrease appears linear.

The suction surface α distribution remains relatively constant at all radial stations up to approximately 60% chord from the leading edge, when a more pronounced increase is noticed. At all stations except the tip, this increase extends to approximately 85% chord and then α decreases toward the trailing edge. This is possibly due to the blade blockage effect in this region. At the tip, α increases continuously and no decrease is noted. Again, as in the pressure surface distribution, α decreases continuously from hub to tip at practically all axial locations, and at some locations the variation appears linear.

In most instances, the magnitudes of α on the suction surface are lower than at the corresponding position on the pressure surface. The deviation between pressure and suction surface measurements decrease continuously with increasing radius from hub to tip. The magnitude of α, which is an indication of the extent of radial flows, is much higher than the values of a single blade reported in Ref. 9. This indicates that the radial

velocity in the inducers are quite appreciable, especially near the blade surfaces.

Velocity Profiles at Station A:

The axial, radial, relative tangential and total relative velocity components derived from hot wire measurements are described in this section.

Fig. 9a shows the tangential variation of the total relative velocity (Q_R) across the inducer passage at several radii. A distinct velocity deficiency is noted at approximately 55% from the blade suction surface for all radial stations, but it is especially pronounced near the tip. This is the interaction region, where the radial flows inside the pressure and suction surface boundary layers, when encountered by the annulus wall, tend to roll towards mid-passage, interact, and produce strong vortices and radially inward flow as explained in Ref. 1. A concentration of high turbulence level in this region is confirmed by measurements described later. The tangential (relative) velocity profile, plotted in Fig. 9b, shows the same trend as Q_R thus indicating the dominance of relative tangential velocity in inducers. Earlier results taken from a pitot tube (Ref. 1 - Fig. 12) do not indicate any deficiency in velocity at mid-passage. In view of the highly turbulent nature of the flow in this region, the pitot tube measurements may be in error at this location. The values of Q_R and V are found to be nearly same as design values from hub to mid-radius and considerably different from mid-radius to tip. The relative velocities near the tip region are much lower than design values resulting in large stagnation (absolute) pressure rise in this region. This large pressure rise is not due to flow turning but are caused by complex mixing and viscous interactions.

From the velocity profiles of Fig. 9a, it is easy to discern the edge of the suction surface boundary layer at radii above R = .671. The suction surface boundary layer appears to grow in thickness as the tip is approached, increasing to approximately 25% of the passage width. This observation is consistent with the previous discussion about tip boundary layer interaction. No evidence of the pressure surface boundary layer can be detected in Fig. 9a. This tends to indicate that the suction surface boundary layer is thicker than that of the pressure surface, although it should be remarked that no measurements were taken close to the blade surface. Since the blade element is not radial, the hot wire probe could not be located very close to the blade surface.

Fig. 9c shows the axial velocity (W) variation across the passage width. The axial velocity is fairly uniform across the channel up to R = 0.781. Beyond R = 0.781, it shows a tendancy to increase towards pressure surface. The radial variation of the axial velocity shows the largest values occurring near the hub, decreasing consistently towards the tip. This tends to indicate the effect of blade blockage on the axial velocity distribution. It is noted from Fig. 9c that negative values of W occur at the tip location R = .973. The existence of negative axial velocities at the extreme tip location indicates the presence of the annulus wall boundary layer scraping effect and was similarly noted by limiting streamline angle measurements at this location reported earlier.

In Fig. 9d is shown the tangential variation of radial velocity U. Large values of radial outward velocity are found near the suction surface at radii close to the hub and negative radial velocities are found near the tip ($R \geq 0.781$), appearing at approximately 45% of the passage width. This is consistant with the previous discussion on boundary layer

interaction in this region. Maximum radial outward velocities are likely to occur near the blade surface and this trend can be discerned from Fig. 9d. Near the hub, the radial velocities are induced mainly by flared hub and blade blockage, since the boundary layer is thin in this region as explained in Ref. 9. From mid-radius to tip, the radial flows are induced mainly by viscous and rotational effects. The radial velocities are of the same order of magnitude as the axial velocity, thus confirming the extent of three dimensionality in the flow.

The total relative velocity distribution obtained from the viscid analysis is shown in Fig. 10a. The imposition of the boundary condition which defines the relative velocity on the inducer blade surface as zero enables the viscid program to provide a crude approximation for the pressure and suction surface boundary layers. The magnitudes of Q_R are similar to those found from the inviscid analysis, except near the blade surfaces. A slight velocity deficiency is noted near the tip at approximately 50% passage width. This agrees with the experimental results of Fig. 9a and indicates an area of high viscous loss. Both inviscid and viscid analyses are compared with hot wire data in Fig. 10b for R = 0.973 and Fig. 10a for R = 0.548. Away from the blade surface, prediction of Q_R from both the analyses are same and agrees reasonably well with the experimental data. Near the blade surface, the viscid analysis should provide better agreement with data. But there is no data available in this region to check the accuracy of the viscid analysis. It is also evident that the viscid analysis tends to over predict the extent of boundary layer growth near the hub. This is due to approximations involved in the viscid analysis as explained later.

The axial velocities predicted from viscid and inviscid analysis at R = .973 and R = .548 are shown compared with experimental results in

Fig. 10d. The predictions are found to be very similar at all radii. The predictions are good at R = .548 and poor at R = .973, thus indicating the dominance of viscous effects near the tip. No comments can be made with regard to the accuracy of viscid results, since the measurements close to the proximity of the wall are not available.

The radial velocities predicted from theoretical analyses are found to be very small in this region and the agreement between the theory and the experiment is only qualitative.

Velocity Profiles at Station B:

The tangential variation of the total relative velocity Q_R is shown in Fig. 11 for the axial station B and at various radial locations. Again, as in station A, a region of distinct velocity deficiency near the mid-passage is noted from mid-radius to tip. The velocity defect has increased considerably (at most of the radii) from that measured at station A. In comparison with the results of station A (Fig. 9a), the position of the maximum velocity defect appears to have shifted towards the suction surface to approximately 40% of the passage width. The measured values of Q_R are much lower than the design values at this location, except near the hub, indicating the extent of three dimensional inviscid and viscid effects.

The tangential variation of the axial velocity W is plotted in Fig. 11 . Overall magnitudes are higher than those measured at station A (Fig. 9c) due to converging annulus. Again, as in station A, the maximum values occur near the hub radius and decrease continuously towards the tip. The decrease in axial velocity near the tip indicates the continuing presence of the annulus wall boundary layer scraping effect. The effect, however, is not as severe as at station A, where negative velocities were measured

(Fig. 9c). It is also evident that the blade boundary layer increase in thickness as the tip is approached.

The variation of radial velocity U across the passage is shown in Fig. 11 . The overall magnitudes appear larger than at station A. The three-dimensional flow effects will be greater at station B and therefore accounts for the greater deviation of the flow from the two-dimensional design values which has been observed at this location. Fig. 11 indicates negative radial velocities for the radii near the tip at approximately 25% from the suction surface. The radially inward flow at this location agrees with the previous discussions on boundary layer interaction and flow mixing which result in the velocity deficiencies and flow loss experienced in this region.

The viscid analysis prediction for the total relative velocity distribution is shown in Fig. 12a. It is a striking departure from the inviscid analysis distribution (Ref. 4) especially near the tip where the viscous effects are known to be appreciable. The viscid analysis also provides crude approximations for the suction and pressure surface boundary layers. A large velocity deficiency near the tip is predicted at approximately 50% passage width and agrees favorably with the experimental Q_R profiles plotted in Fig. 11 . It is apparent that the velocity deficiency noted near the tip at station A (Fig. 10) has grown considerably as the flow proceeded downstream to station B indicating an increase in size and intensity of the viscous loss region and substantiating the experimental results discussed previously. The blade boundary layer development predicted by the viscid analysis can be seen in Fig. 12a. The suction surface boundary layer appears comparable in magnitude to the pressure surface boundary layer, both of which increase in thickness from hub to tip. The velocity gradients

near the suction surface boundary layer is steeper indicating the effect of adverse pressure gradients on this surface.

Experimental and theoretical comparisons of Q_R distribution at R = 0.973 and 0.548 are given in Figs. 12b and 12c respectively. It appears that the viscid analysis distribution provides better agreement with experiment, especially at the tip. The magnitude as well as the trend is predicted reasonably well.

Fig. 12d shows the axial velocity distribution predicted from both inviscid and viscid analyses compared with the experiment at R = 0.671 and 0.973. The viscid analysis reveals the approximate profiles inside the suction and pressure surface boundary layers. At R = 0.671 the predictions from viscid analysis agree better with experiment. While, near the tip, the predictions are poor from both the theories, especially near the pressure surface. The decrease in axial velocity from hub to tip is predicted and this is in agreement with the data.

The magnitude of radial velocities predicted from both inviscid and viscid analyses are found to be consistantly lower than the experimental values.

Passage Averaged Velocities:

The passage averaged values of measured total relative velocity ($\bar{Q}_R$), axial velocity ($\bar{W}$) and radial velocity ($\bar{U}$) at stations A, B and at the exit are plotted and compared with the corresponding predictions from inviscid and viscid analyses in Fig. 13. It is evident from Fig. 13a that the prediction of $\bar{Q}_R$ is poor at axial station A and reasonably good at station B. There is considerable decrease in $\bar{Q}_R$ towards the tip at station B and this is predicted more accurately by the viscid analysis. The descrepancy between the design values (not shown) and the experimental data is found

to be large, especially at station B, thus indicating the need to incorporate the dominant three-dimensional invescid and viscid effects in the prediction of the flow in inducers. The descrepancy between design and measured values of $\bar{Q}_R$ is as much as 50% (design $\bar{Q}_R = 0.88$, measured $\bar{Q}_R = 0.4$ at $R = 0.975$) near the tip, a consequence of appreciable boundary layer growth and mixing in this region.

The passage averaged axial velocities ($\bar{W}$) at stations A and B are shown in Fig. 13b. The measured values show a rapid decrease in axial velocity towards the tip at station A. This trend is predicted by viscid analysis. The agreement between theory and experiment is very good at station B. The magnitude of $\bar{W}$ increases from station A to B, an effect of converging annulus. Again, as in station A, the distribution of $\bar{W}$ shows larger values near the hub indicating the continuing presence of blade blockage, which is large at this radial location. It is interesting to note that the opposite trend is observed in the measurements taken downstream of the trailing edge (Fig. 5 - station C) and plotted in Fig. 13d. As shown in Fig. 13d, the axial velocities are very low at the hub (back flow region) and very high near the tip. This implies that significant changes occur in the axial velocity profile as the flow leaves the inducer passage. These changes may be responsible, in part, for the back flow region shown in Fig. 13d.

In Fig. 13c are shown the passage averaged radial velocities compared with viscid and inviscid analyses. At stations A and B, the measured radial velocities are of the same order of magnitude as the axial velocities, further confirming our conclusion that the flow in inducers in highly three-dimensional. The radial velocities are higher near the hub (mostly caused by blade blockage and flared hub) and decrease slightly towards

the tip. Furthermore, the average radial velocity increases continuously from leading to trailing edge. The predictions are qualitative at station B. One possible reason for the poor prediction at station B is that the real fluid effects are not accurately accounted for in our analyses. The turbulent stresses are found to be very high in this region, even away from the blade surfaces as discussed later, and this is not taken into account in the viscid analysis developed in this paper.

In Fig. 13d, the passage averaged values of absolute tangential velocity ($\bar{V}_\theta$) and axial velocity ($\bar{W}$) at the trailing edge location are compared with the experimental data at station C shown in Fig. 5. At the hub, the prediction of $\bar{V}_\theta$ is poor. Near mid-radius, the inviscid analysis seem to provide better agreement. The viscid analysis provides better qualitative agreement near the tip. The steep rise in $\bar{V}_\theta$ towards the tip is predicted, qualitatively, by the viscid analysis. Axial velocities predicted by both viscid and inviscid analyses are almost similar (not shown). Here again the agreement between the theory and the experiment is good only in the middle third of the annulus. One cannot expect the axial velocities shown in Fig. 13d to be predicted accurately, unless the three-dimensionality and viscous effects in the wake are accurately simulated in the viscid analysis presented in this paper.

Turbulence Intensities:

The distributions of radial, tangential and axial intensities at station B, non-dimensionalized with respect to local total relative velocity, are shown in isocontour form in Fig. 14. The contours for all three intensity components are essentially the same, showing a "pocket" or "core" of high turbulence centered at approximately 40% passage width and R = .890. This coincides with the location of the maximum total relative velocity deficiency

noted in Fig. 11. The turbulence intensities are generally higher than those encountered in a stationary passage. The peak intensities occur in the mixing region near the tip, where the two boundary layers merge and generate considerable flow mixing. The flow energy dissipated during this process is responsible for the velocity deficiencies encountered near the tip region in Fig. 11. Another concentration of high turbulence is noted near the hub pressure surface and is an indication of the proximity to the pressure surface boundary layer.

The radial component of turbulence intensities $\sqrt{\overline{u^2}}$ are generally higher than those in axial and tangential directions. This observed behaviour is opposite to known behaviour in stationary passages, where the streamwise component is the dominant one, and $\overline{v^2} > \overline{w^2} > \overline{u^2}$. It can be shown, using the turbulent energy equation in rotating coordinates, that the rotation (or the coriolis forces) has marked effect on turbulence characteristics. Anand (7) has shown that in compressors and pumps, where the direction of rotation is opposite to that of the relative flow, the terms due to rotation yield an extra production term in the transport equation for $\overline{u^2}$, resulting in increased turbulence intensities in the radial direction. Anand's (7) experiment also confirms the trend observed here, namely, $\overline{u^2} > \overline{v^2} > \overline{w^2}$.

It should be remarked that all the measurements reported here were taken away from the blade surfaces. The maximum turbulence intensities and stresses are likely to occur near the blade surfaces. High turbulence intensities measured away from the blade surfaces and reported here reflect the extent of turbulent mixing even near the mid-passage. The classical assumption that the viscous and turbulence effects are confined to very thin regions near the blade surface is evidently inapplicable to inducers

and hence, a fully three-dimensional treatment is needed for the prediction of inducer flows.

Turbulence Stresses:

The distribution of turbulence velocity correlations $\overline{vw}$, $\overline{uw}$ and $\overline{uv}$ were measured at station B using the method described in Ref. 10. What is required from the point of view of practical application is the shear stress in the cylinderical plane, τ_s, (in the direction of resultant velocity $\sqrt{V^2 + W^2}$) and radial direction, τ_r, as shown in Fig. 1. The measured correlations ($\overline{vw}$, $\overline{uw}$ and $\overline{uv}$) can be used to find τ_s and τ_r as follows

$$\tau_s = -\rho\overline{v_n v_s} = \overline{(w\cos\beta + v\sin\beta)(v\cos\beta - w\sin\beta)}$$

$$= \overline{(v^2 - w^2)\sin\beta\cos\beta} + \overline{vw(\cos^2\beta - \sin^2\beta)} \qquad (11)$$

where,

$$\sin\beta = \frac{V + v}{\sqrt{(V+v)^2 + (W+w)^2}}, \quad \cos\beta = \frac{W + w}{\sqrt{(V+v)^2 + (W+w)^2}} \qquad (12)$$

v_s and v_n are fluctuating velocities in the direction of velocity V_s ($= \sqrt{V^2 + W^2}$) and normal directions respectively (Fig. 1).

Substituting equations (12) in (11) and neglecting second order terms compared to mean velocities we get

$$\tau_s = -\frac{\rho}{V^2+W^2}\left\{VW(\overline{v^2} - \overline{w^2}) + \overline{vw}(W^2 - V^2)\right\} \qquad (13)$$

similarly the turbulence stress in the radial direction is given by

$$\tau_r = -\rho\overline{uv}_n = -\rho\ \overline{u(v\cos\beta - w\sin\beta)}$$

$$\simeq -\frac{\rho}{\sqrt{V^2+W^2}}\left(\overline{uv}\ W - \overline{uw}\ V\right) \qquad (14)$$

The values of τ_s, τ_n and $|\tau|$ so derived are plotted in Fig. 15. Concentration of turbulence stresses are similar to turbulence intensity contours plotted in Fig. 14. The maximum stresses occur in the mixing region near the tip (from R = 0.78 to 0.973) at approximately 40% passage width.

The values of τ_s follows the same trend, qualitatively, as the velocity profiles of Q_R plotted in Fig. 11 . Near the suction surface, away from the wall, the velocity gradients are negative resulting in negative value of stresses. Maximum stresses occur at R = 0.89 and near 30% passage width, this location corresponds to maximum velocity gradients (Fig. 11). The turbulence stress ($|\tau|/\rho Q_R^2$) measured near the wall of flat plate at zero incidence is of the order of 1.5×10^{-3}. It is evident that the stresses measured (Fig. 15a) in a rotating inducer passage from mid-radius to tip, away from the wall, is of the same order of magnitude and is in fact 2 to 4 times higher than this in some locations. This is one of the significant results of this investigation. More accurate estimate of the stresses within the channel is essential for the accurate prediction of the flow using viscid theory.

The radial component of stresses are by far the most dominant ones as shown in Fig. 15b. As mentioned earlier, the stresses shown are away from the blade surface and their values near the blade surfaces are likely to be much higher. The radial stresses follow the same trend as the radial velocity gradients (note the correspondence between velocity gradients and τ_r at R = 0.973 and 0.945 at 20% passage point). One can prove qualitatively

(Ref. 7), using Reynolds stress equation in rotating coordinates, that the effect of rotation is to increase turbulent stresses in the radial direction and suppress it in the streamwise direction. It is also evident that the total shear stress vector is not parallel to the resultant velocity vector. This is contrary to what is normally assumed in the analysis of three-dimensional turbulent boundary layer.

The resultant stress $(\tau)(=\sqrt{\tau_s^2+\tau_r^2})$ are plotted in Fig. 15c. The ratio $(|\tau|/\rho\overline{q^2})$, where $\overline{q^2}$ is the total turbulence energy is found to vary from 0.04 to 0.27, with values averaging 2 in the region of higher stresses. In some boundary layer computations, the turbulence modelling is based on the assumption that the ratio of (stress/intensity) is constant, which is true only for isotropic turbulence. That this is not true is evident from this investigation.

DISCUSSION AND CONCLUSIONS

It should be remarked here that the viscid analysis carried out in this paper is a first attempt ever to solve for the real fluid effects in turbomachinery passage using the entire equations of motion. It is a logical extension of Cooper and Bosch program, which, we think, was a breakthrough in the three-dimensional inviscid analysis of turbomachinery flows. Further improvements and refinements of the viscid analysis presented in this paper are needed before the three-dimensional flow field can be predicted accurately. It is evident from the data reported, especially the shear stress measurements, that the shear stresses are non zero even at mid-passage and the resultant stress vector is not necessarily parallel to the resultant velocity vector. If the analysis could be modified to incorporate these effects, the prediction of velocity components, especially

the radial component (which is not predicted accurately in this paper) could be vastly improved. Some of the major conclusions of this paper are;

(1) The viscid analysis, even though approximate, provides better prediction of the three-dimensional flow field, especially near the trailing edge. More tangential grid stations would be needed to better define the shape of the three-dimensional boundary layer.

(2) The limiting streamline angle measurements indicate large radial velocities near the blade surfaces increasing gradually from leading edge to trailing edge. Negative values of α at the pressure surface tip indicate radially inward flow due to annulus wall boundary layer scraping effect.

(3) The measured blade static pressures agree with the theory, except near the suction surface of the blade tip.

(4) Total relative velocity measurements indicate substantial velocity deficiency at the outer radius near mid-passage, indicating complex interaction between blade boundary layer and annulus wall. This is responsible for high stagnation pressure (absolute) size measured at the exit of the inducer near the outer radius.

(5) Inside the passage, the axial velocities are generally higher near the hub and lower at the tip. This trend is reversed as the flow proceeds downstream of the trailing edge. A slight backflow is observed at the tip near the leading edge.

(6) The measured radial velocities are found to be of the same order of magnitude as the axial velocity. A region of radially inward flow is found near the tip region at mid-passage.

(7) Turbulence intensities are generally much higher than those encountered in stationary passages, especially near the tip. The radial

components turbulence intensity is found to be highest and this effect can be attributed to rotation.

(8) The streamwise and radial components of turbulence stresses are found to be very high, especially in the tip region. The radial stresses are higher than the streamwise components and this effect can be attributed to rotation.

REFERENCES

1. Lakshminarayana, B., "Three Dimensional Flow Field in Rocket Pump Inducers; Part 1: Measured Flow Field Inside the Rotating Blade Passage and at the Exit," J. Fluids Engineering, p. 567, Dec. 1973.

2. Cooper, P., and Bosch, H., "Three Dimensional Analysis of Inducer Fluid Flow," NASA Report CR-54836, TRW ER-6673A, February 1966.

3. Poncet, A. and Lakshminarayana, B., "Investigation of Three Dimensional Flow Characteristics in a Three Bladed Rocket Pump Inducer," NASA Report CR-2290, 1973.

4. Gorton, C. A., "Analytical and Experimental Study of Mean Flow and Turbulence Characteristics Inside the Passages of an Axial Flow Inducer," M. S. Thesis, The Pennsylvania State University, 1974, (also as PSU Aersp. Report 74-2).

5. Giesing, J. P., "Extension of the Douglas-Neumann Program to Problems of Lifting, Infinite Cascades," Douglas Aircraft Division Report LB-31653, July 1964.

6. Lakshminarayana, B. and White, M. T., "Airfoil in a Contracting or Diverging Stream," J. of Aircraft, Vol. 9, No. 5, pp. 354-360, May 1972.

7. Anand, A. K., "An Experimental and Theoretical Investigation of Three Dimensional Turbulent Boundary Layers Inside the Helical Passages of a Turbomachinery Rotor," Ph.D. Thesis, Dept. of Aerospace Engineering, The Pennsylvania State University, 1975.

8. Lakshminarayana, B., "Experimental and Analytical Investigation of Flow Through a Rocket Pump Inducer," Fluid Mechanics and Design of Turbomachinery, NASA SP 304, 1974.

9. Lakshminarayana, B., Jabbari, A., and Yamaoka, H., "Turbulent Boundary Layer on a Rotating Helical Blade," J. Fluid Mech., Vol. 51, Part 3, pp. 545-569, 1972.

10. Gorton, C. A., Lakshminarayana, B., "A Method of Measuring the Three Dimensional Mean Flow and Turbulence Quantities Inside a Rotating Turbomachinery Passage," ASME Paper 75-GT-4 (to be published J. Engr. for Power).

LIST OF FIGURES

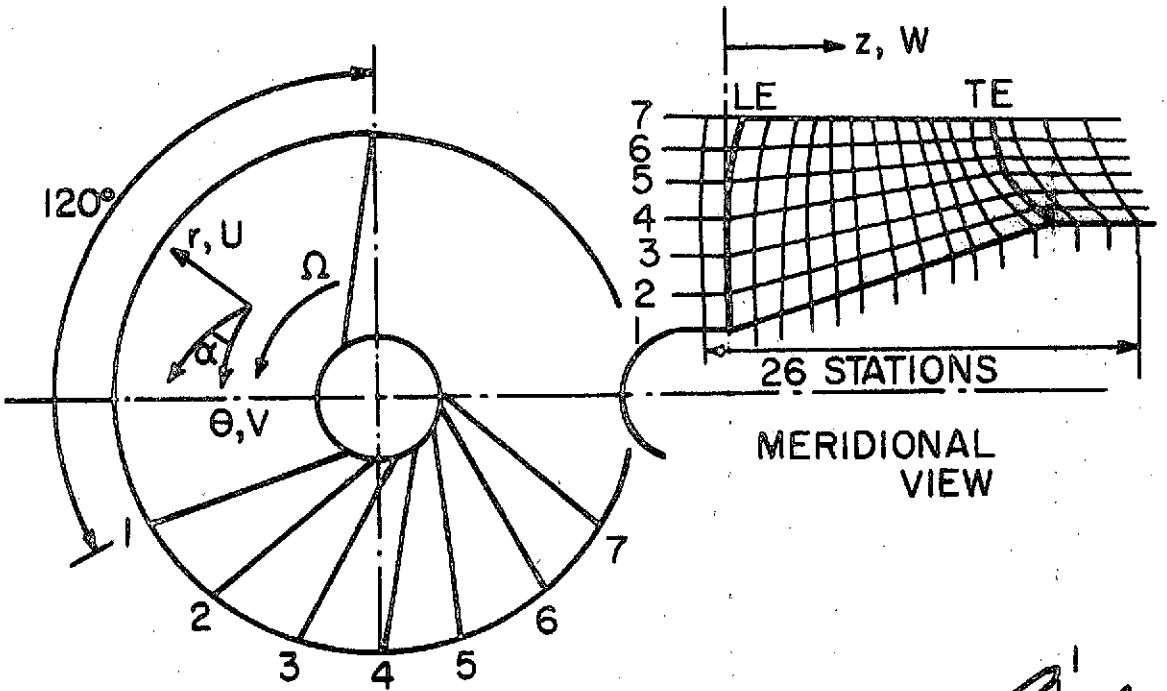
z, W
LE
TE
7
6
5
4
3
2
1
26 STATIONS
MERIDIONAL VIEW
120°
r, U
Ω
α
θ, V
1
2
3
4
5
6
7
VIEW INTO INLET
1
4
7
323°
DEVELOPED VIEW OF SECTIONS 1,4,7
r, U, u
n, Vn, vn
τs
qR
θ, V, v
β
s, Vs, vs
Z, W, w
τr
(Vs = √(V²+W²))

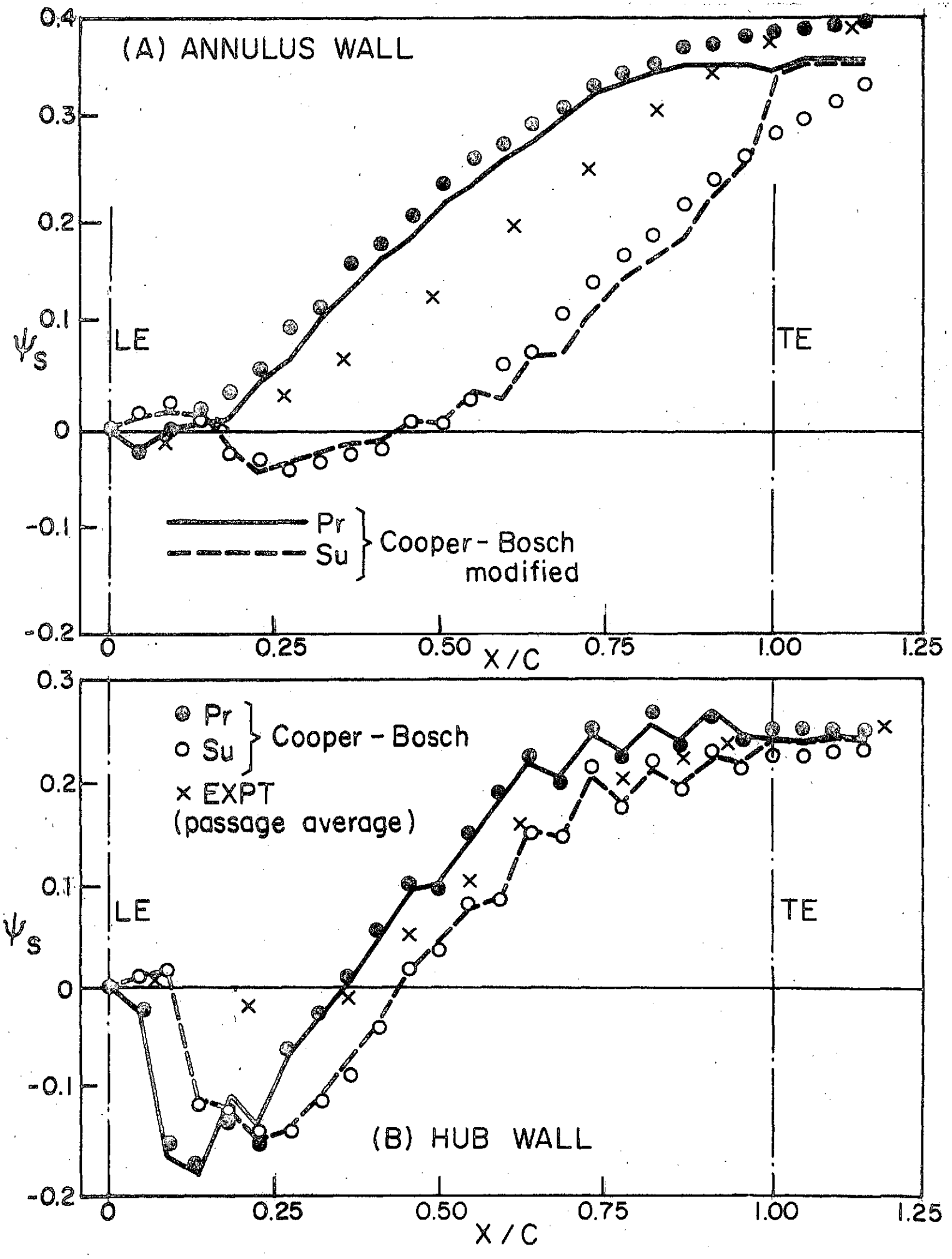
(A) ANNULUS WALL
0.4
0.3
0.2
0.1
0
-0.1
-0.2
ψ_s
LE
TE
Pr
Su
Cooper - Bosch modified
0
0.25
0.50
0.75
1.00
1.25
X / C
0.3
0.2
0.1
0
-0.1
-0.2
Pr
Su
Cooper - Bosch
× EXPT
(passage average)
LE
TE
ψ_s
(B) HUB WALL
0
0.25
0.50
0.75
1.00
1.25
X / C

FIGURE 9

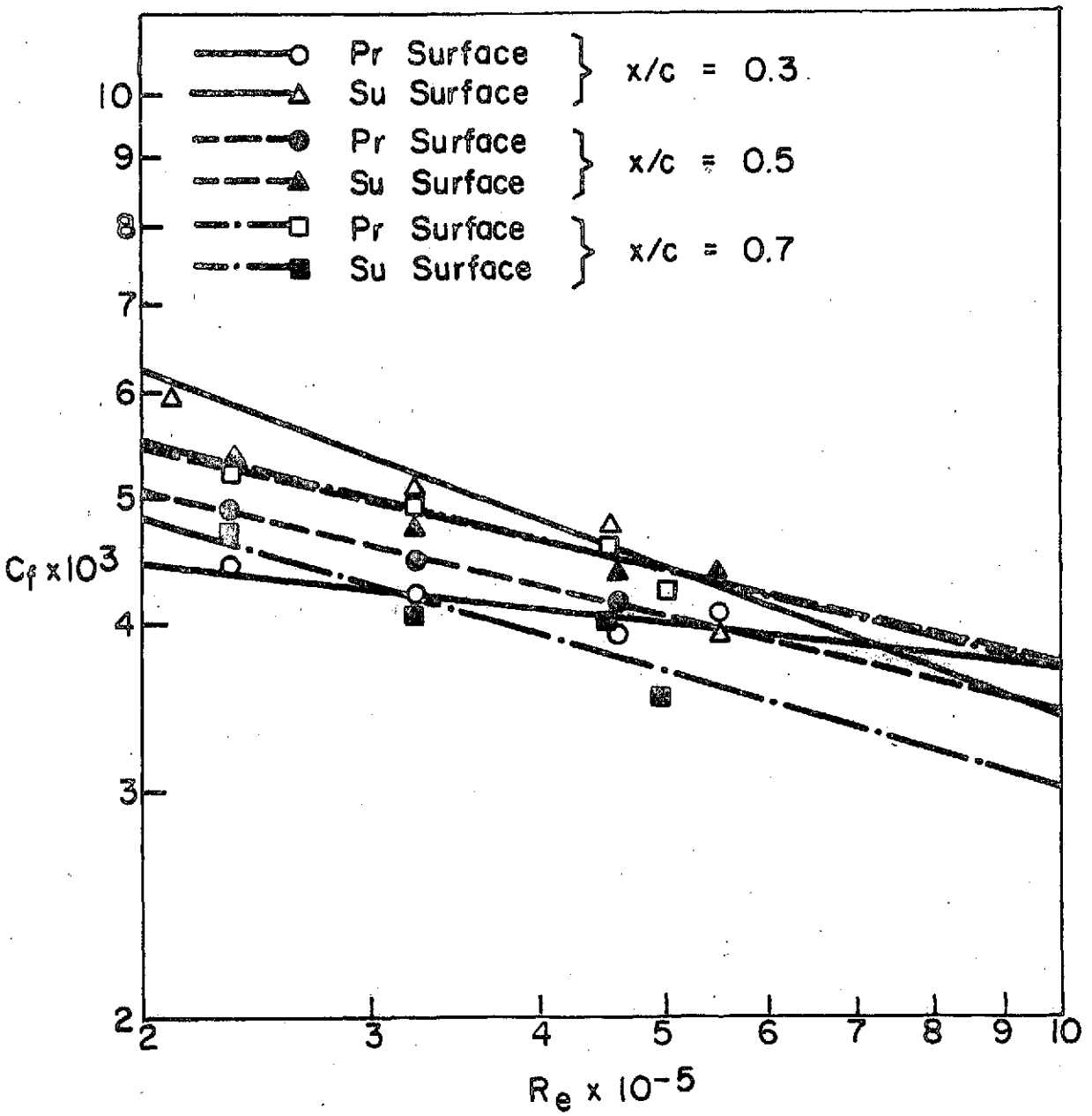
Pr Surface
Su Surface
x/c = 0.3
Pr Surface
Su Surface
x/c = 0.5
Pr Surface
Su Surface
x/c = 0.7
$C_f \times 10^3$
$R_e \times 10^{-5}$
10
9
8
7
6
5
4
3
2
2
3
4
5
6
7
8
9
10

FIGURE 3

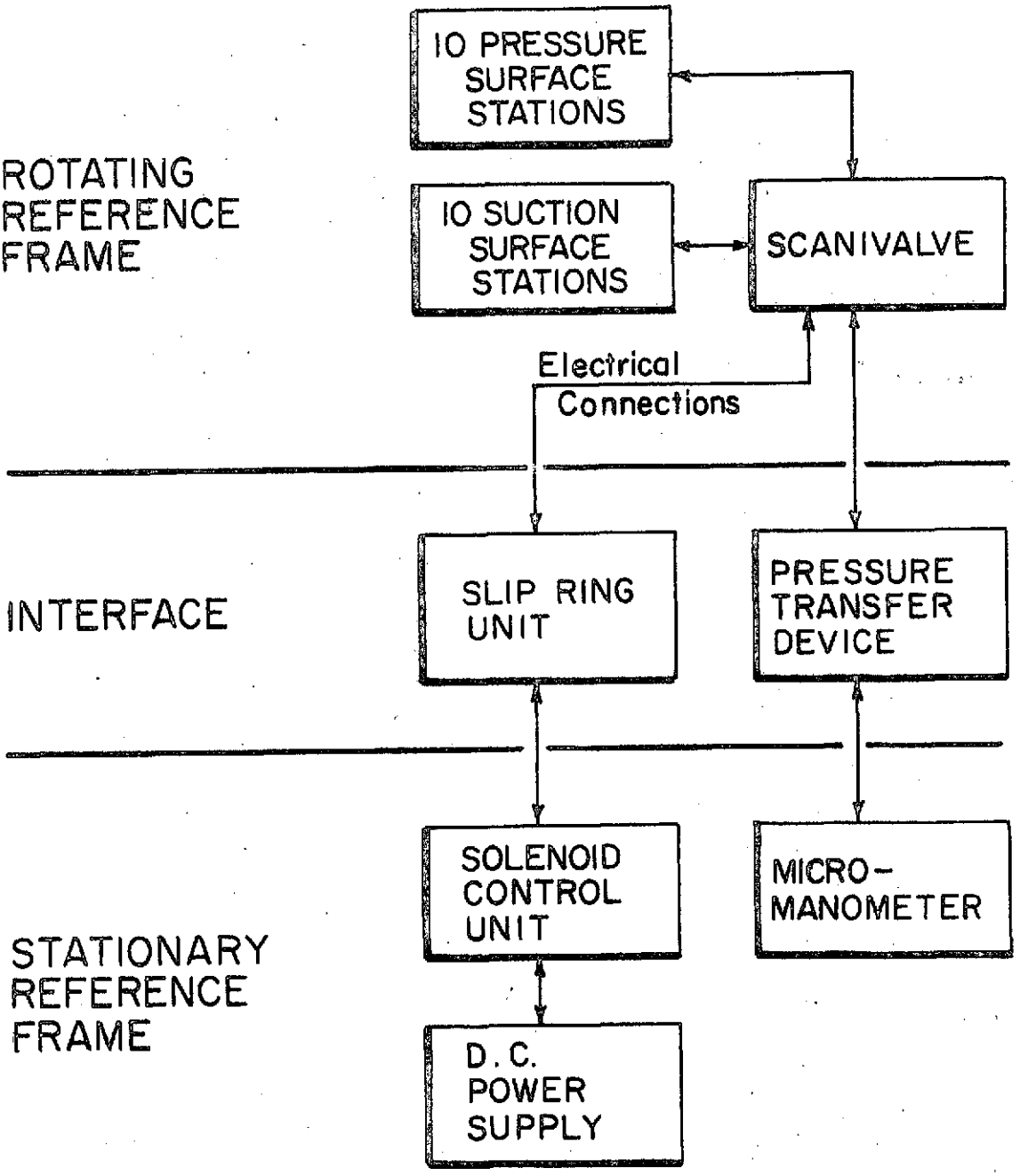
10 PRESSURE SURFACE STATIONS
ROTATING REFERENCE FRAME
10 SUCTION SURFACE STATIONS
SCANIVALVE
Electrical Connections
INTERFACE
SLIP RING UNIT
PRESSURE TRANSFER DEVICE
SOLENOID CONTROL UNIT
MICRO-MANOMETER
STATIONARY REFERENCE FRAME
D.C. POWER SUPPLY

FIGURE -4-

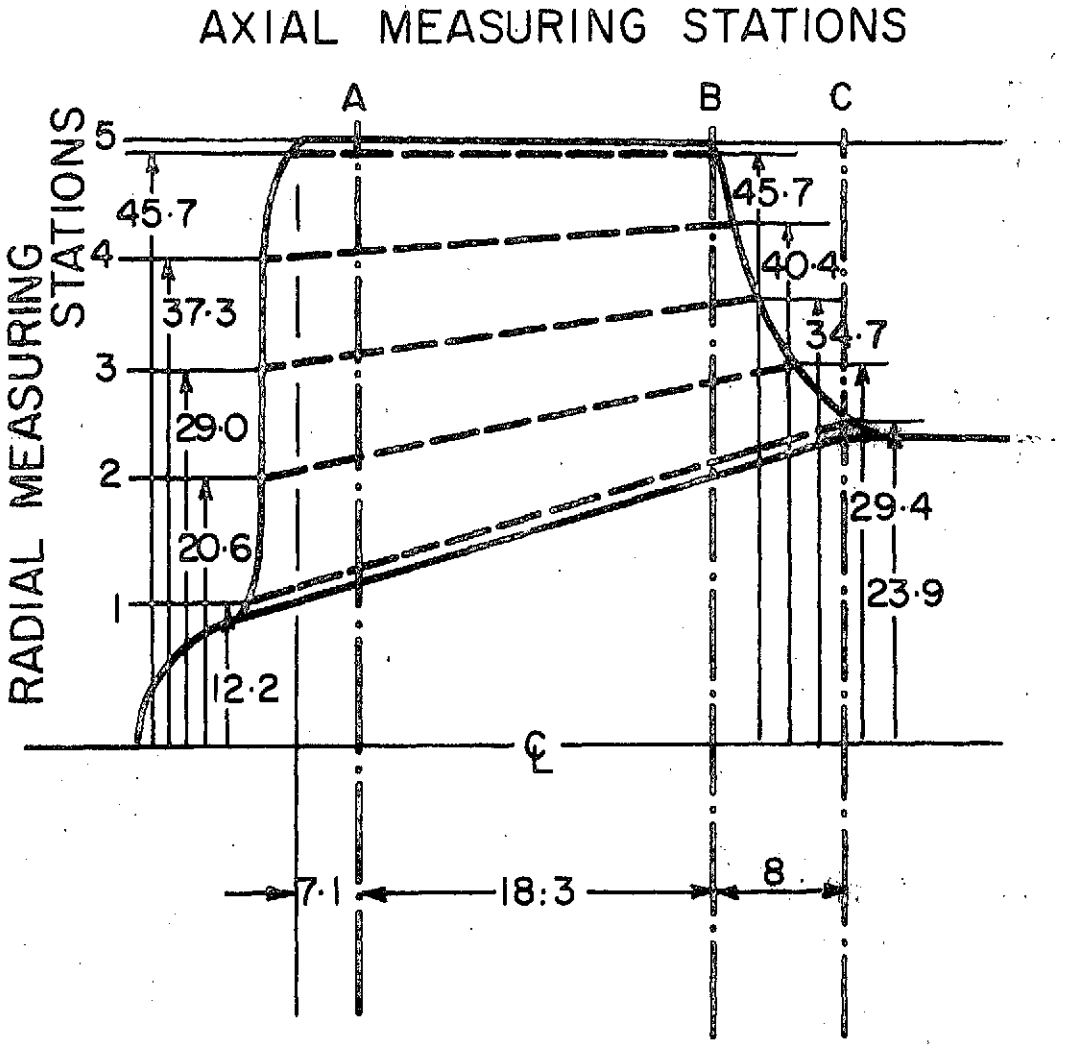
AXIAL MEASURING STATIONS
A
B
C
RADIAL MEASURING STATIONS
5
4
3
2
1
45·7
37·3
29·0
20·6
12·2
45·7
40·4
34·7
29·4
23·9
℄
7·1
18·3
8
Static pressure and limiting streamline angle measurements
Flow survey stations
(all measurements are in cm.)

FIGURE 5

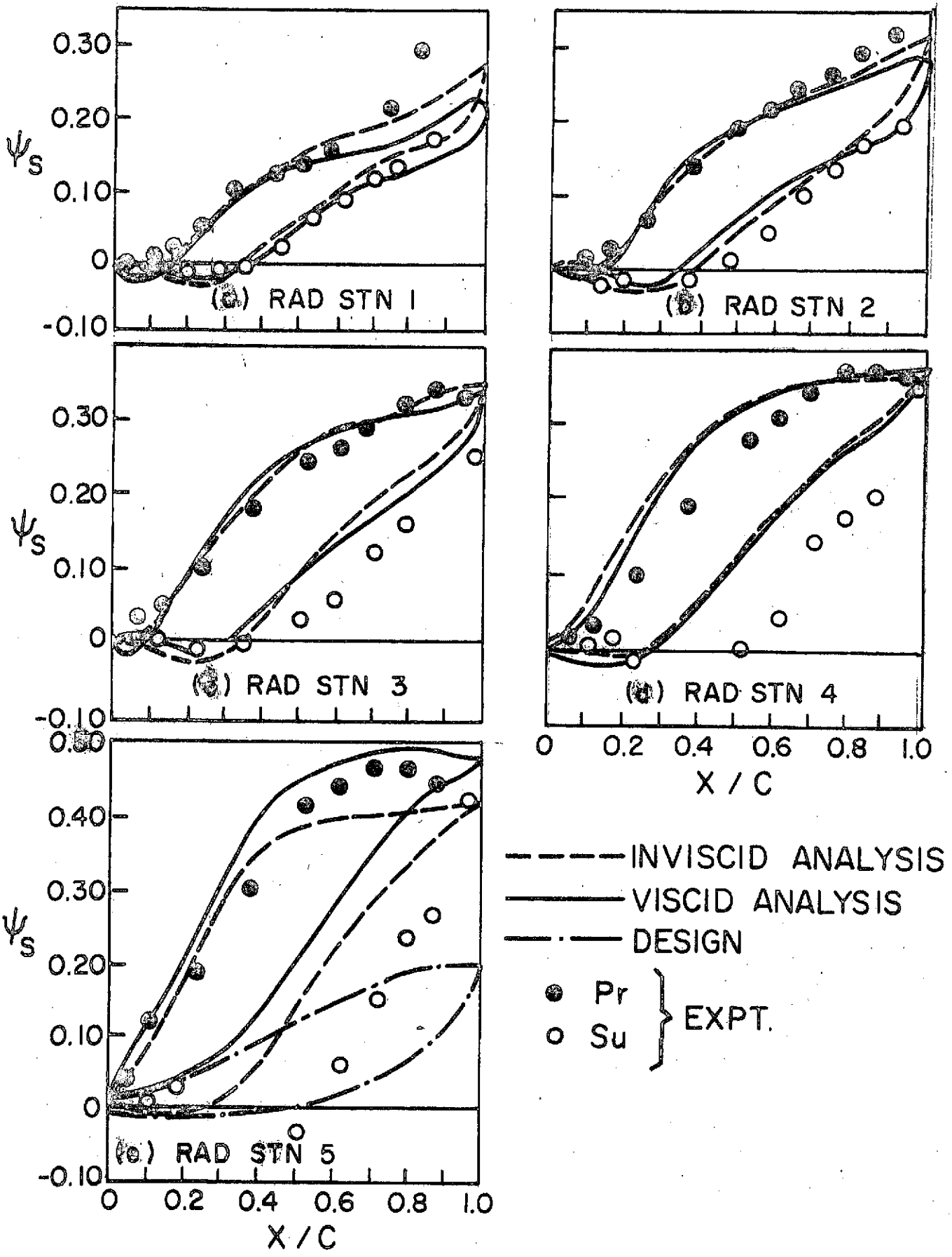
0.30
0.20
0.10
0
-0.10
ψ_s
(a) RAD STN 1
(b) RAD STN 2
(c) RAD STN 3
(d) RAD STN 4
(e) RAD STN 5
0.50
0.40
0.30
0.20
0.10
0
0.2
0.4
0.6
0.8
1.0
X / C
INVISCID ANALYSIS
VISCID ANALYSIS
DESIGN
Pr
Su
EXPT.

FIGURE 6

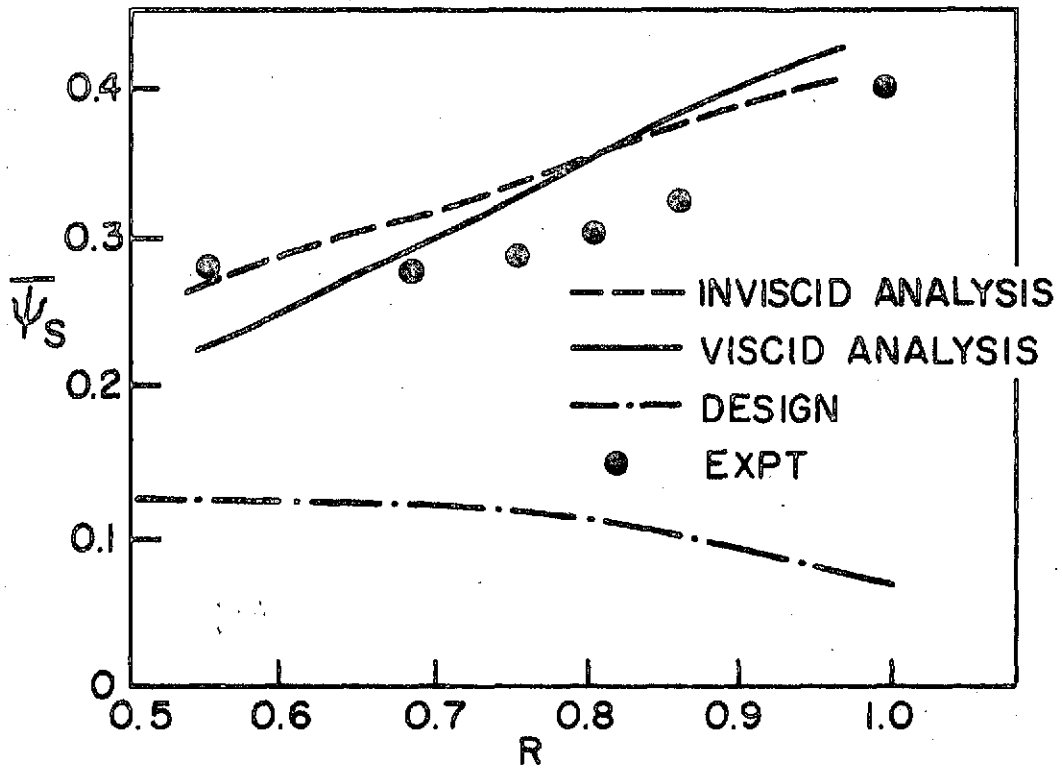

(a) STATION C

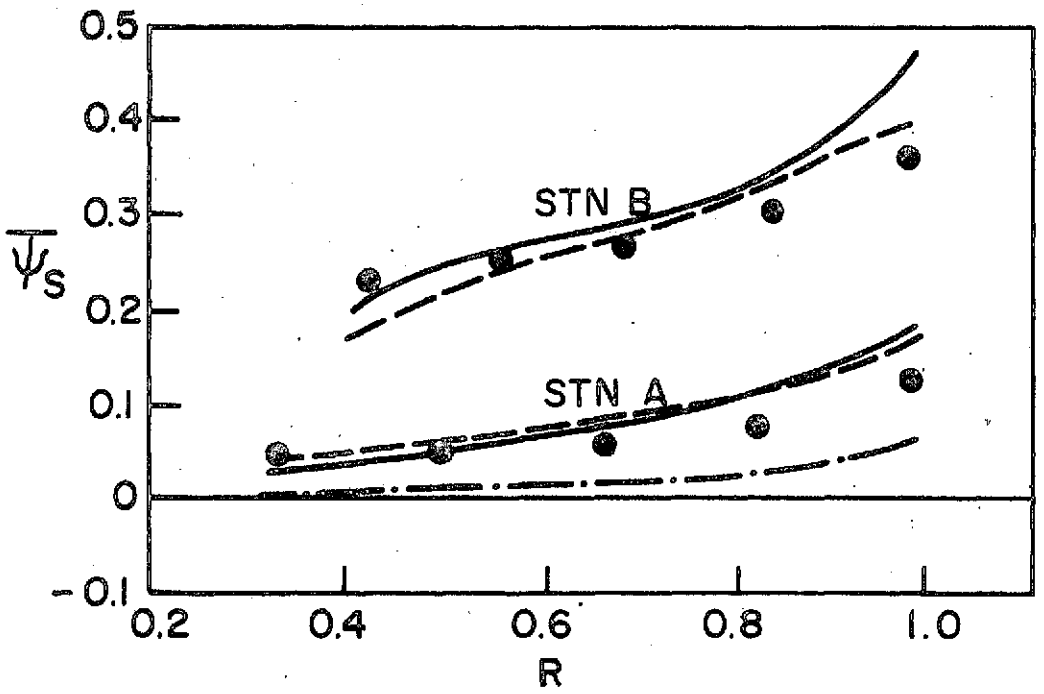

(b) STATIONS A & B

FIGURE 7

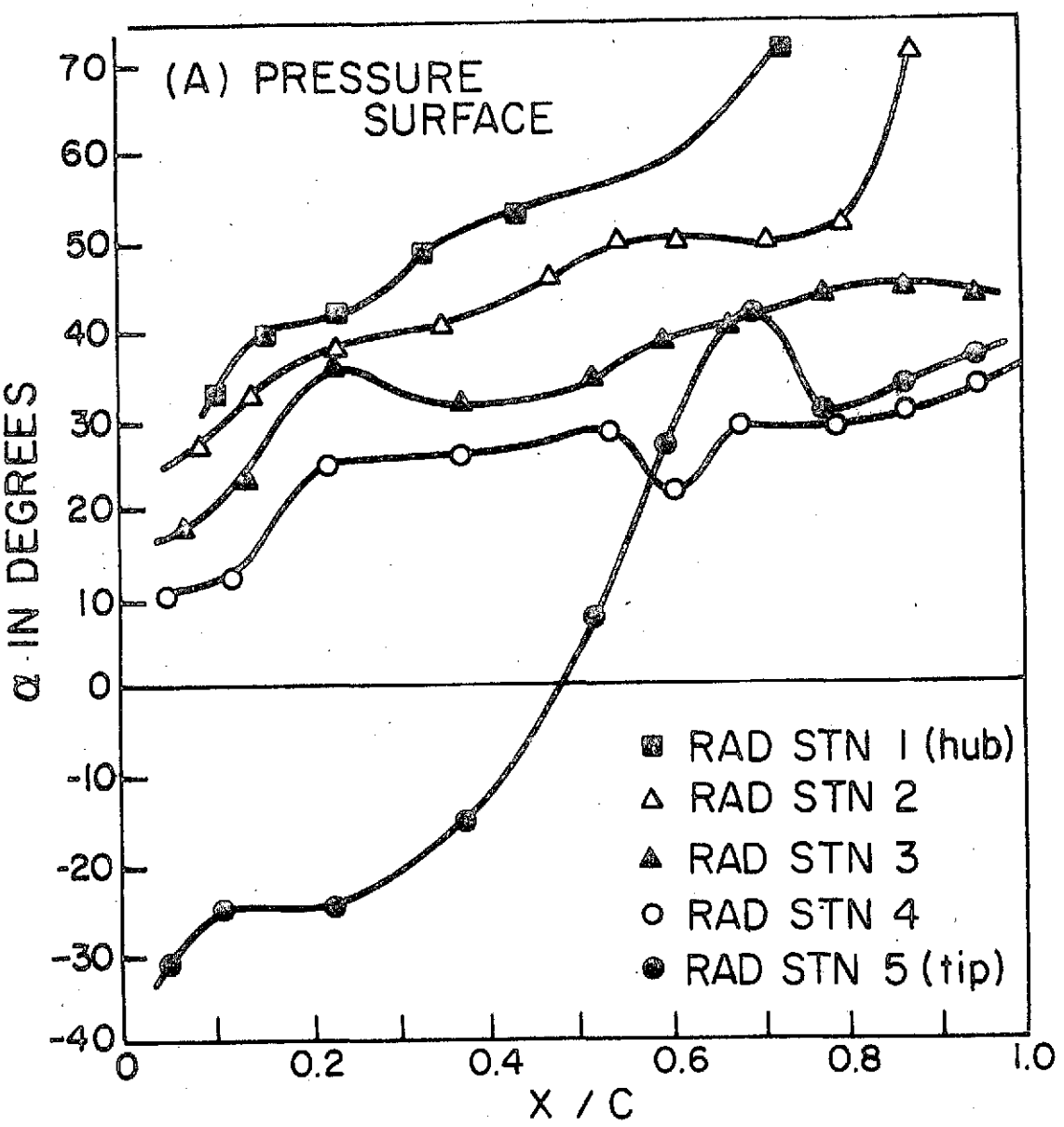
(A) PRESSURE SURFACE
α IN DEGREES
70
60
50
40
30
20
10
0
-10
-20
-30
-40
0
0.2
0.4
0.6
0.8
1.0
X / C
RAD STN 1 (hub)
RAD STN 2
RAD STN 3
RAD STN 4
RAD STN 5 (tip)

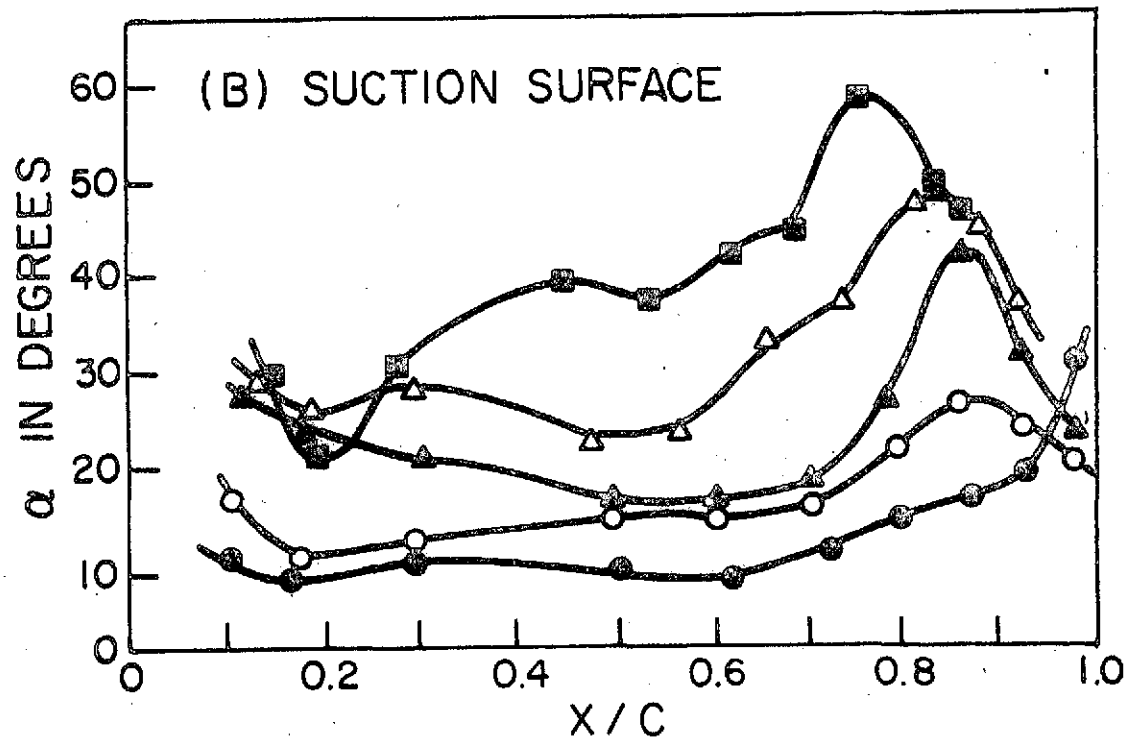
(B) SUCTION SURFACE
α IN DEGREES
60
50
40
30
20
10
0
0
0.2
0.4
0.6
0.8
1.0
X / C

Fig 8

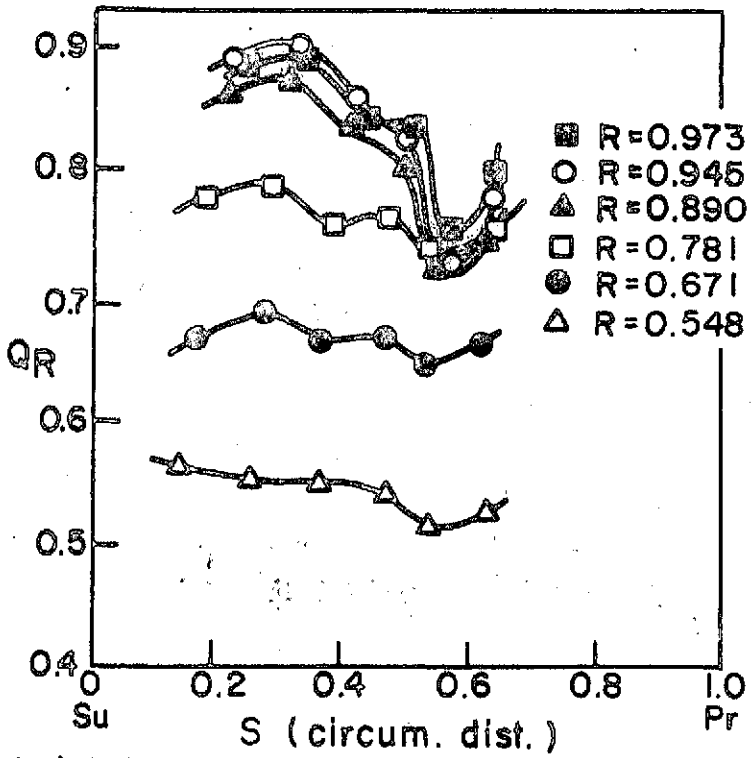

(a) TOTAL RELATIVE VELOCITY (Q_R)

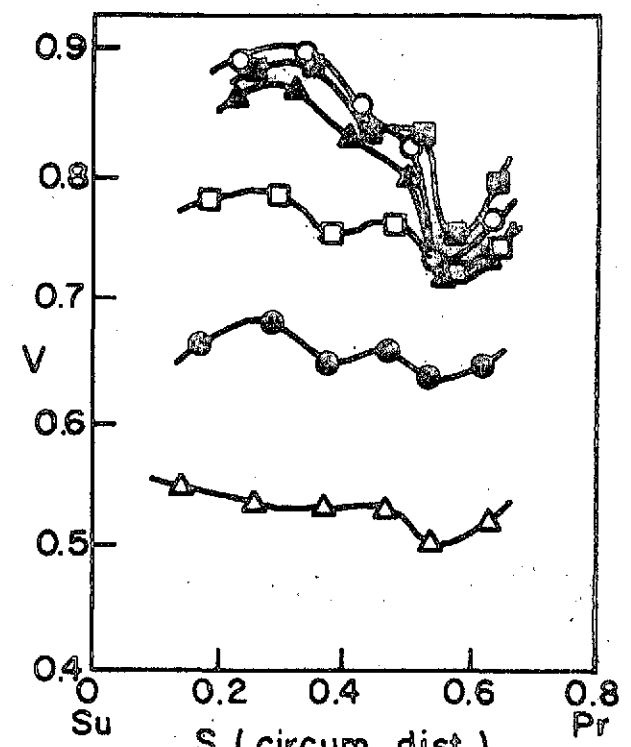

(b) RELATIVE TANGENTIAL VELOCITY (V)

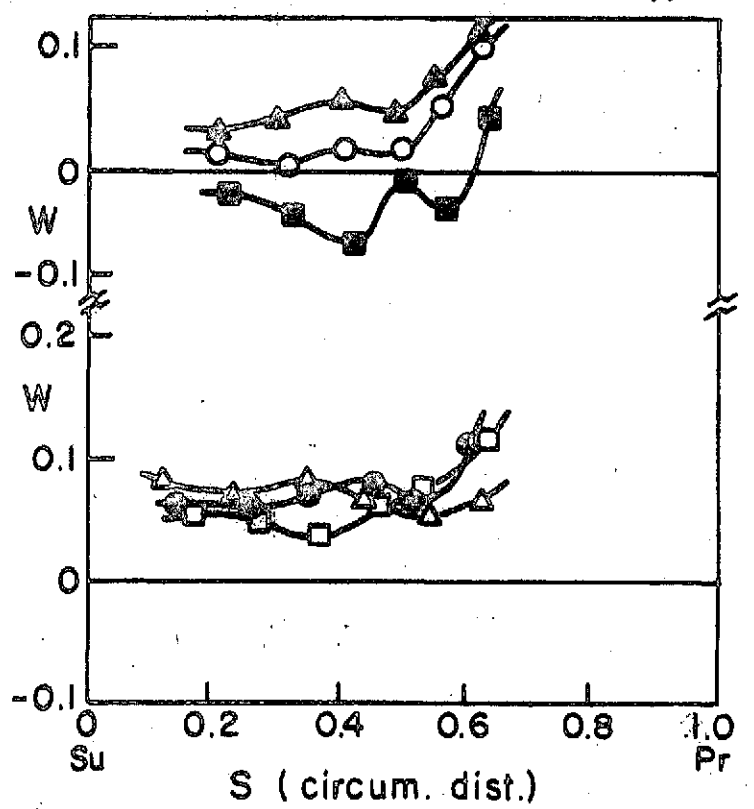

(c) AXIAL VELOCITY (W)

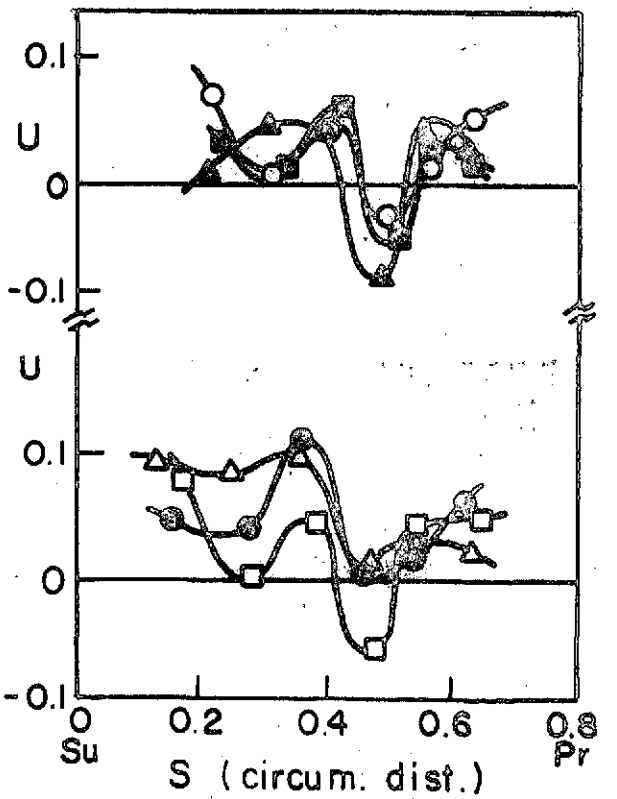

(d) RADIAL VELOCITY (U)

FIGURE 9

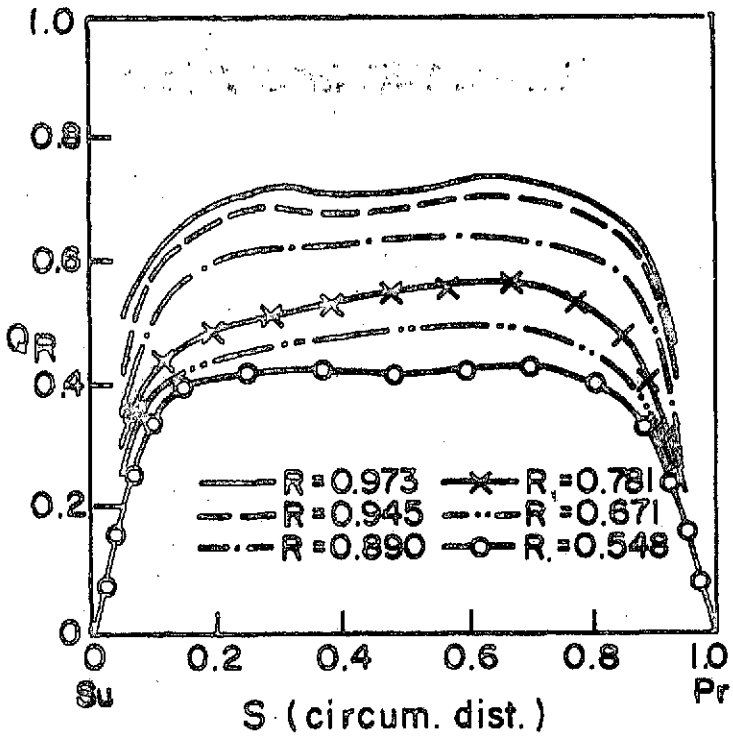

(a) Q_R FROM VISCID ANALYSIS

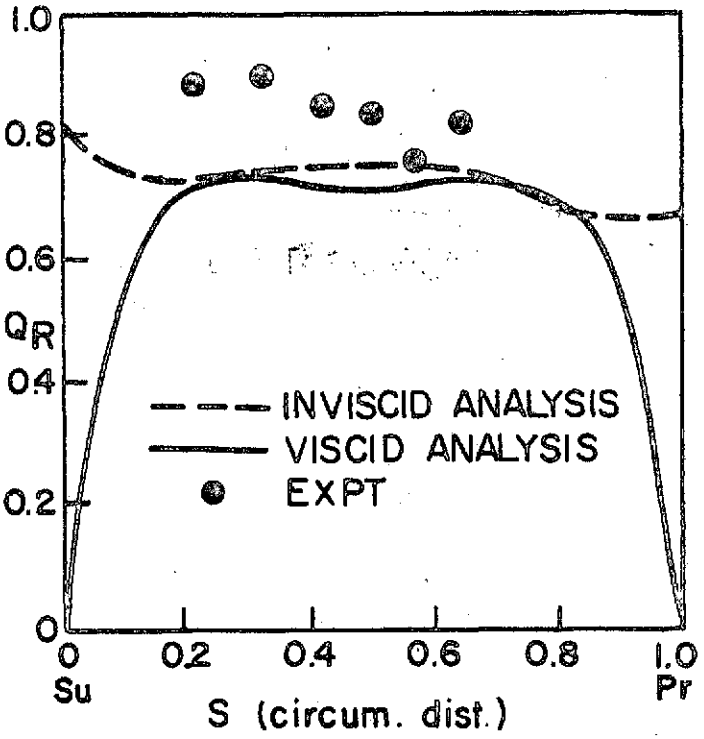

(b) Q_R AT R=0.973

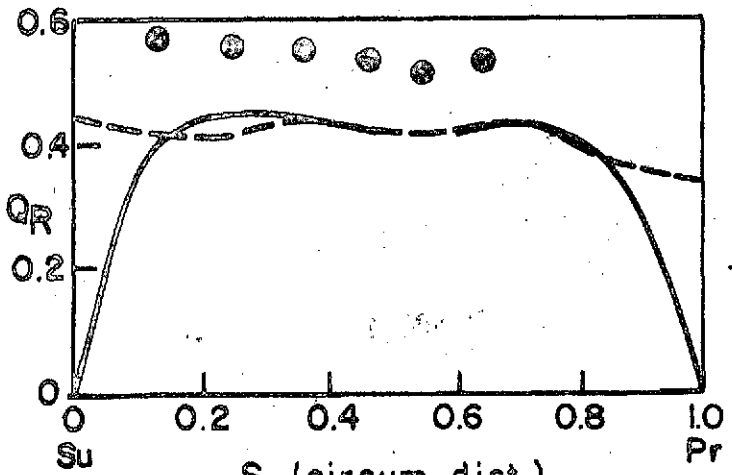

(c) Q_R AT R=0.548

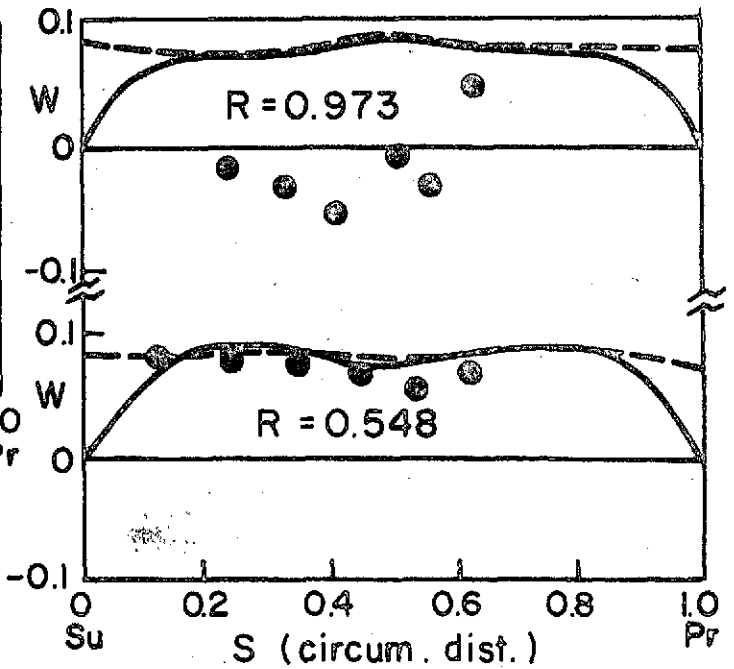

(d) W AT R=0.973 & R=0.548

FIGURE 10

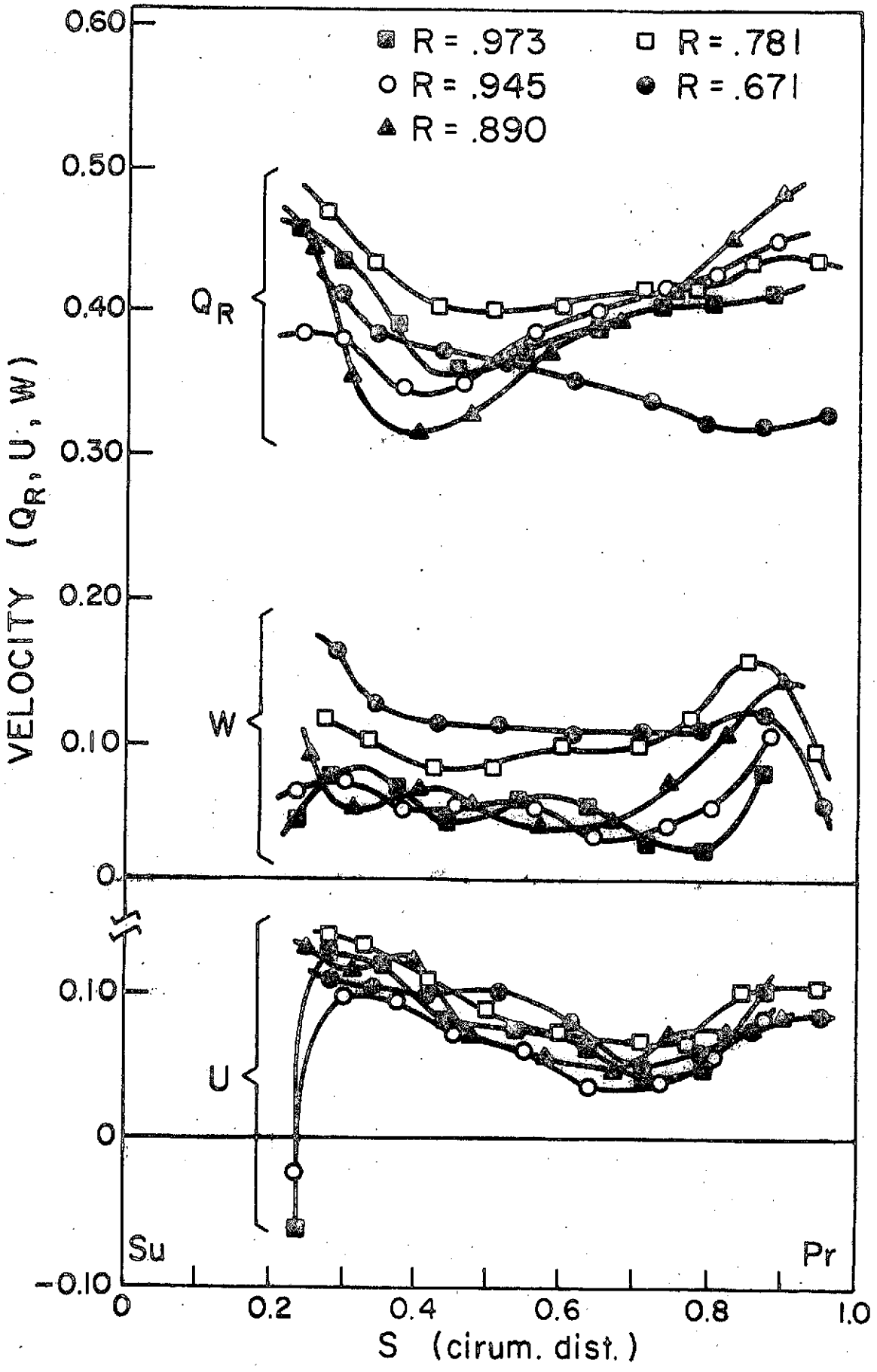
R = .973
R = .945
R = .890
R = .781
R = .671
Q_R
W
U
VELOCITY (Q_R, U, W)
0.60
0.50
0.40
0.30
0.20
0.10
0
0.10
0
-0.10
Su
Pr
0
0.2
0.4
0.6
0.8
1.0
S (cirum. dist.)

FIGURE 11

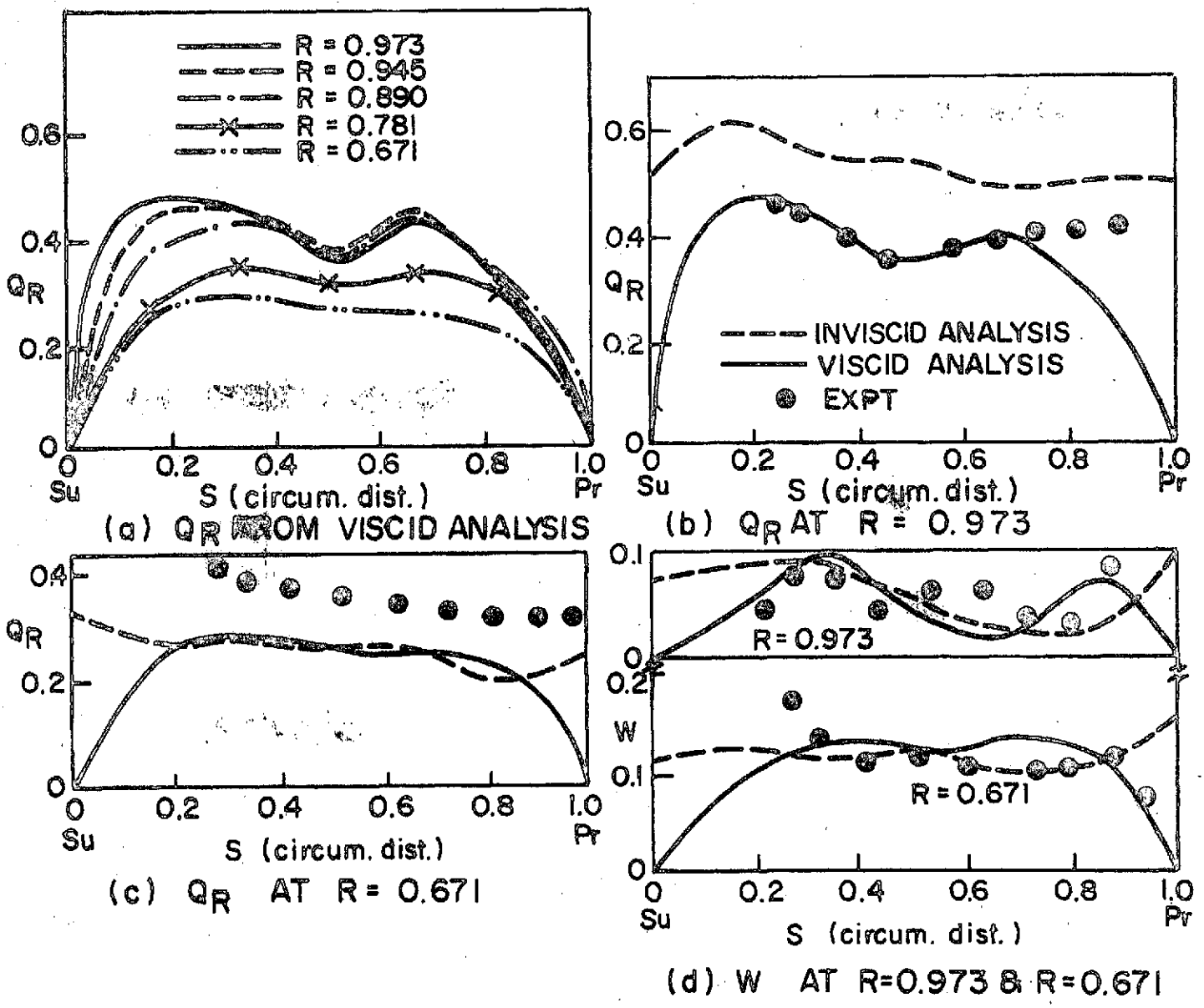
R = 0.973
R = 0.945
R = 0.890
R = 0.781
R = 0.671
Q_R
0.6
0.4
0.2
0
0
0.2
0.4
0.6
0.8
1.0
Su
Pr
S (circum. dist.)
(a) Q_R FROM VISCID ANALYSIS
INVISCID ANALYSIS
VISCID ANALYSIS
EXPT
(b) Q_R AT R = 0.973
(c) Q_R AT R = 0.671
W
0.1
R = 0.973
R = 0.671
(d) W AT R=0.973 & R=0.671

FIGURE 12

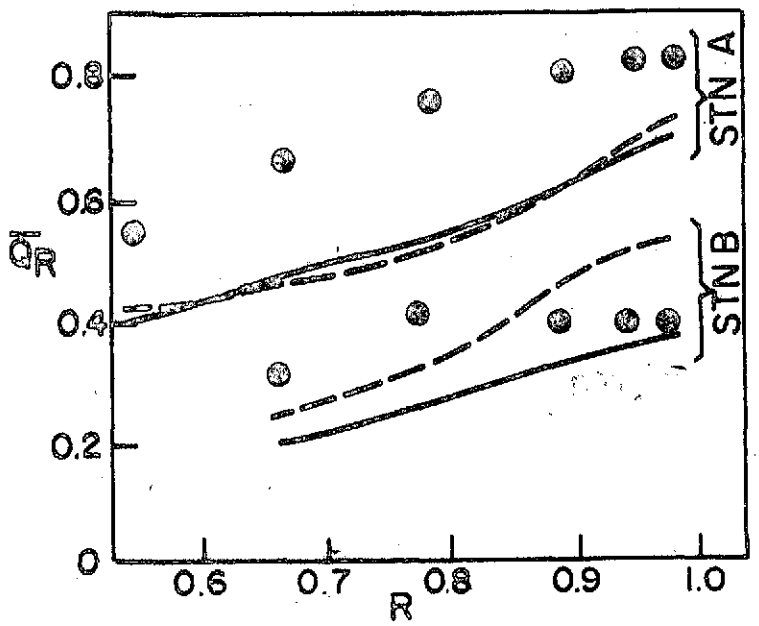

(a) $\overline{Q}_R$ AT STATIONS A & B

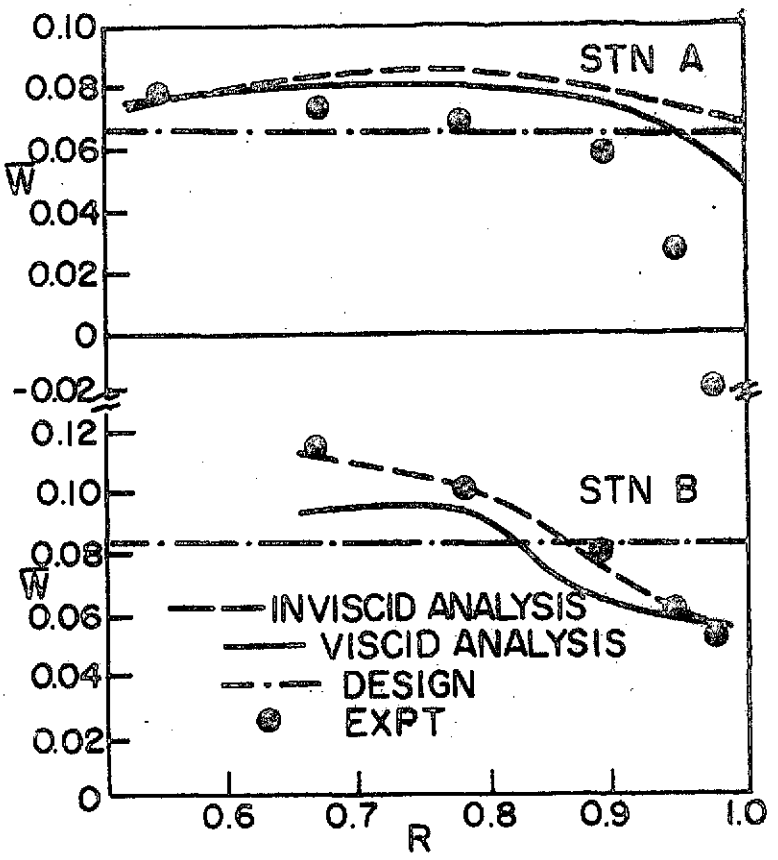

(b) $\overline{W}$ AT STATIONS A & B

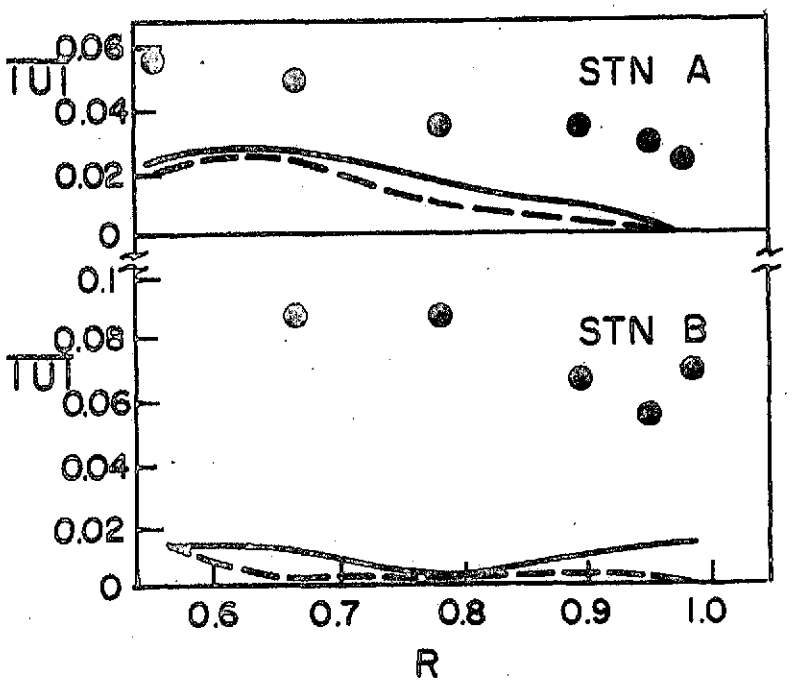

(c) $\overline{U}$ AT STATIONS A & B

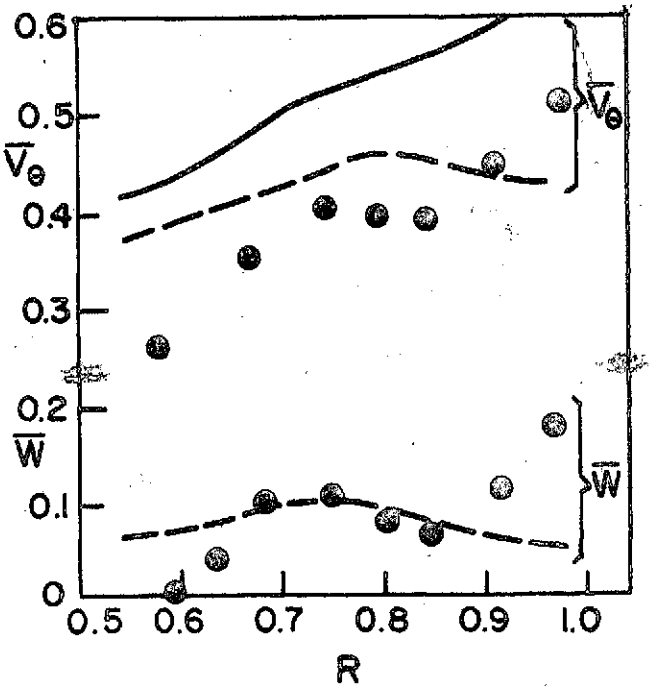

(d) $\overline{V}_\theta$ & $\overline{W}$ AT STATION C

FIGURE 13

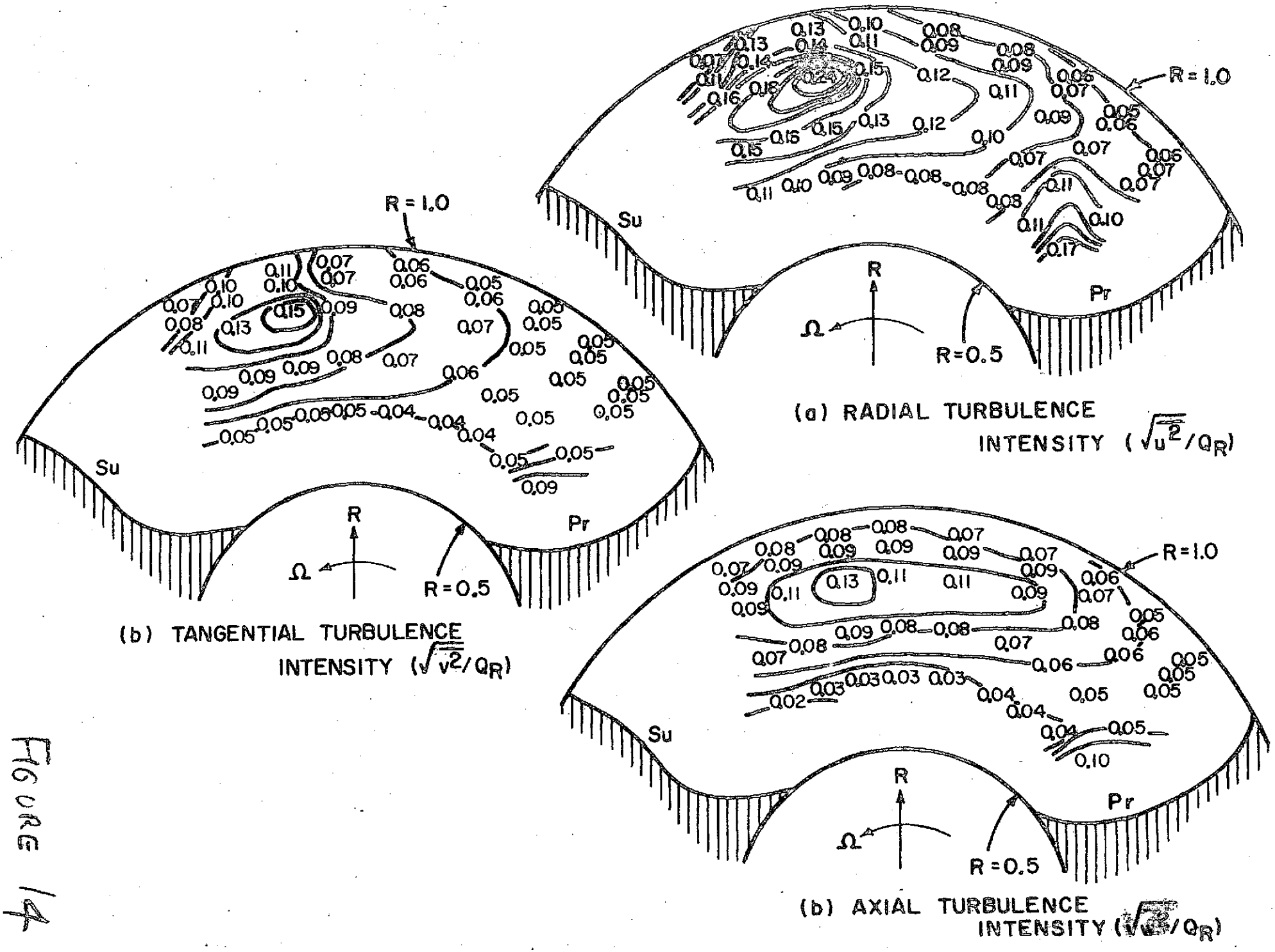
R = 1.0
Su
Pr
R
Ω
R = 0.5
(a) RADIAL TURBULENCE INTENSITY ($\sqrt{u^2}/Q_R$)
(b) TANGENTIAL TURBULENCE INTENSITY ($\sqrt{v^2}/Q_R$)
(b) AXIAL TURBULENCE INTENSITY ($\sqrt{w^2}/Q_R$)

FIGURE 14

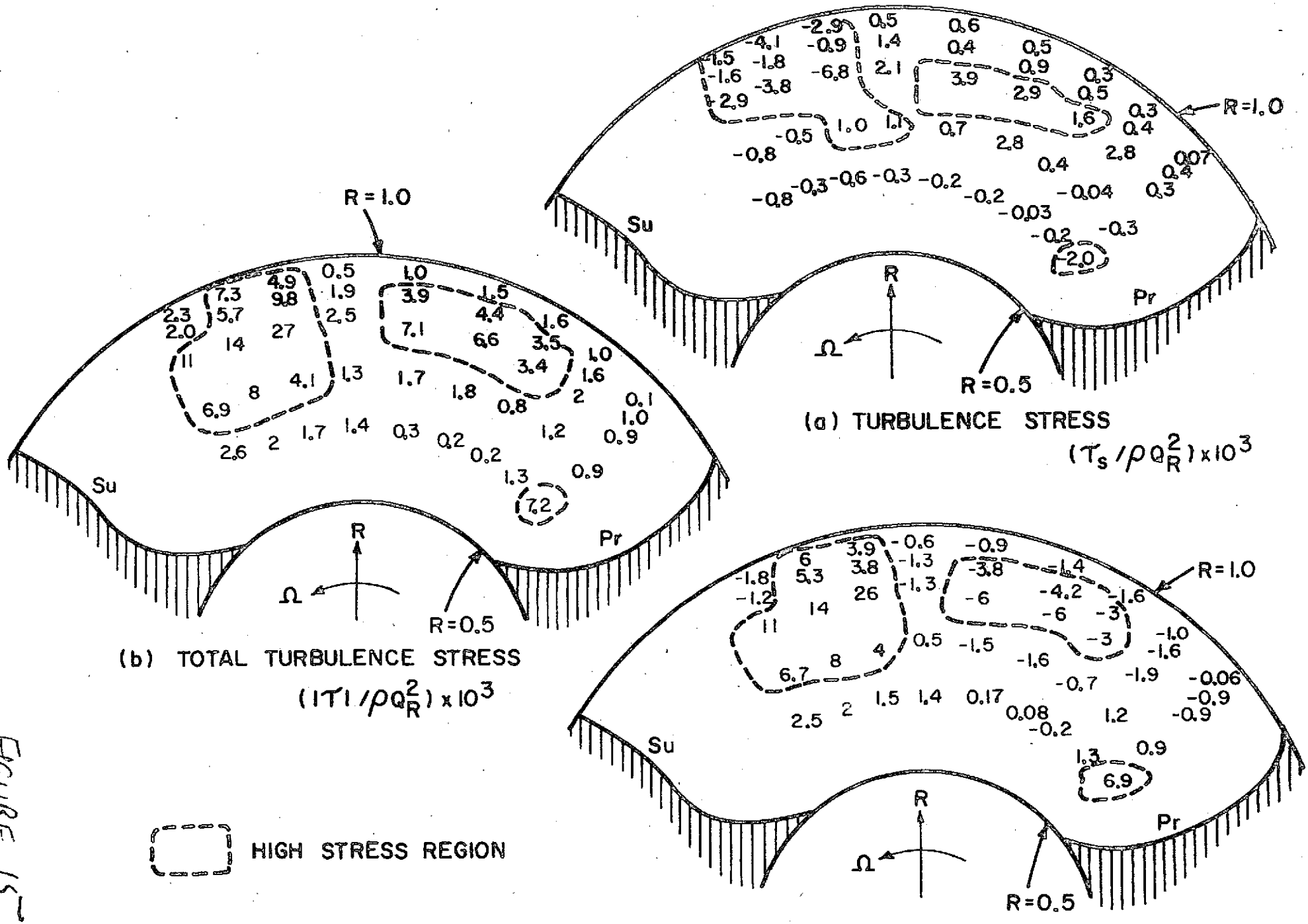
R = 1.0
R=0.5
Su
Pr
R
Ω
(a) TURBULENCE STRESS
$(\tau_s/\rho Q_R^2)\times 10^3$
(b) TOTAL TURBULENCE STRESS
$(|\tau|/\rho Q_R^2)\times 10^3$
(c) TURBULENCE STRESS
$(\tau_r/\rho Q_R^2)\times 10^3$
HIGH STRESS REGION

FIGURE 15